Designed proteins assemble antibodies into modular nanocages

Robert Divine

A dissertation

submitted in partial fulfillment of the

requirements for the degree of

Doctor of Philosophy

University of Washington

2021

Reading Committee:

David Baker, Chair

Neil King

Young Kwon

Program Authorized to Offer Degree:

Biochemistry

University of Washington

Abstract

Designed proteins assemble antibodies into modular nanocages

Robert Divine

Chair of the Supervisory Committee:
David Baker
Department of Biochemistry

Antibodies are widely used in biology and medicine, and there has been considerable interest in multivalent antibody formats that increase binding avidity and enhance signaling. However, general approaches are lacking for forming precisely oriented antibody assemblies with controlled valency. For my doctoral thesis, I computationally designed two-component nanocages that overcome this limitation by uniting form and function. One nanocage component is any suitable antibody or Fc-fusion, and the second is a designed Fc-binding homo-oligomer that drives nanocage assembly. Structures of 8 antibody nanocages match the corresponding computational models, spanning dihedral, tetrahedral, octahedral, and icosahedral architectures with 2, 6, 12, and 30 antibodies per nanocage. Antibody nanocages targeting cell-surface receptors enhance signaling compared to free antibodies or Fc-fusions in DR5-mediated apoptosis, Tie2-mediated angiogenesis, CD40 activation, and T cell proliferation; nanocage assembly also increases SARS-CoV-2 pseudovirus neutralization by α-SARS-CoV-2 monoclonal antibodies and Fc-ACE2 fusion proteins.

Table of Contents

List of Figures

List of Tables

Acknowledgements

I wouldn't have graduated or progressed as a scientist without the generous mentorship of my colleagues. Jorge Fallas and George Ueda took me under their collective wings and shaved years of trial-and-error off my thesis by being the absolute experts in protein nanocage design, purification, and validation techniques; not to mention, both were great friends. Other postdoc mentor-colleagues were essential in helping me grow as a scientist by generously sharing their time and experience: Chad Miller, Yang Hsia, and Jamie Lazarovits deserve special thanks here. I also had the pleasure to work on a cohort-based mentorship project with an unbelievable team of researchers who selflessly volunteered their time to help others: Christine Kang, Alena Khmelinskaia, Kandise VanWormer, and Erin Yang.

Protein design projects don't work without proteins or design. For their amazing ability to express and purify proteins with yields that put me to shame, I'd like to thank: Alex Roederer, Brooke Fiala, Natalie Brunette, Elizabeth Kepl, Lauren Carter, Mike Murphy, and Colin Correnti. On the computational design side, this project would not have been possible without the initial inspiration from Ivan Vulovic, Will Sheffler, and David Baker, as well as the validation work done by Yang Hsia and Rubul Mout. For institutional help, I'd like to thank: Erin Kirschner, Kandise VanWormer, Lance Stewart, Zari Magness, Ratika Krishnamurty, Luki Goldschmidt, Patrick Vecchiato, and Michelle Matsunaga.

I'd like to thank Ha Dang for being my most frequent and long-standing collaborator, for her perpetual honesty about the quality of my EM grid preparation

techniques, and for her championing of this project from its earliest days. I've had the pleasure of working closely with many other collaborators who always lent their expertise and time, and I want to thank Marti Tooley, Ali Etemadih, Julie Mathieu, Shally Saini, Blair Zhao, Infencia Xavier, Peter Morawski, Franziska Seeger, Lexi Walls, Leo Stamatatos, Andy McGuire, Daniel Campbell, Madeleine Jennewein, Leah Homad, Yu-Hsin Wan, Mitch Fahning, and Olivier Poncelet for their support.

David Baker allowed me to work in his lab on a computational protein design project when I had no experience with computers, protein, or design. Thank you for your trust and affirmation. I'd also like to thank the incredible support I've gotten from other professors, such as my committee: Neil King, Young Kwon, Kelly Lee, and David Veesler; my rotation mentors: Joseph Mougous and Hannele Ruohola-Baker; and pre-graduate mentors: Scott Rankin, John Brady, and Alicia Orta-Ramirez.

My research was a collaborative effort with many of the great scientists listed above. Franziska designed and characterized the Fc-binding repeat protein; George and Jorge helped analyze the SAXS data; Ha led the electron microscopy structural efforts; Jamie helped design and conduct the stability and exchange experiments; Shally, Julie, George, and Jorge designed and conducted the DR5 experiments; Blair, Infencia, Hannele, George, Jorge, and Jamie designed and conducted the A1F-Fc experiments; Marti and Neil conducted and designed the CD40 agonist experiments; Peter, Mitch, and Daniel designed and conducted the T cell proliferation assays; Madeleine, Leah, Yu-Hsin, Leo, and Andy designed and conducted the IgG pseudovirus

neutralization studies; and Ha, Lexi, Lance, and David Veesler designed the pseudovirus neutralization studies with Fc-ACE2.

I'm happy to have so many other smart colleagues and friends who helped me throughout my studies, and to name a few: Ryan Kibler, Natasha Edman, Ian Haydon, James Griffin, Gabi Reggiano, Carson Adams, Halli Benasutti, Inez Pranoto, Will White, Will Sheffler, Thad Huber, Gilonne d'Origny, Anindya Roy, Sidney Lisanza, Lukas Milles, Una Nattermann, Christian Richardson, Dan Ellis, Chloe Adams, Jilliane Bruffey, Jorgen Nelson, Sanaa Mansoor, Erika DeBenedictis, Justas Dauparas, Danny Sahtoe, Hanlun Jiang, Jacob O'Connor, Brian Koepnick, Brian Coventry, Hugh Haddox, Shiri Levy, and Kaitlyn Lacourse, among many others.

This work was supported by many generous grants and donations, including: the Audacious Project at the Institute for Protein Design, NSF grant CHE 1629214, the HHMI, the Washington Research Foundation, the Nordstrom-Barrier Directors Fund at the Institute for Protein Design, the Washington State General Operating Fund for the Institute for Protein Design, a Wu Tsai Translational Investigator Fund, the Nan Fung Life Sciences Translational Investigator Fund, NIH/NIDCR grant T90 DE021984 and NIH/NCATS TR002318, the Fred Hutch COVID-19 Research Fund, NIH grant R01AI127726, NIH/NCI Cancer Center Support Grant P30 CA015704, ISCRM Pilot Award, the NIAID/NIH DP1AI158186 and HHSN272201700059C grants, NIGMS/NIH R01GM120553, a Pew Biomedical Scholars Award, a Burroughs Wellcome Investigators in the Pathogenesis of Infectious Diseases award, Fast Grants, the University of Washington Arnold and Mabel Beckman cryoEM center, Amgen for the

AMG-655 antibody, Dr. Akilesh for donating primary tubular epithelial cells, and Dr. Kaelin for donating RCC4 cells. SAXS work was conducted at the Advanced Light Source (ALS), a national user facility operated by the Lawrence Berkeley National Laboratory on behalf of the Department of Energy (DOE), Office of Basic Energy Sciences, through DOE BER IDAT grant (DE-AC02-05CH11231) and NIGMS supported ALS-ENABLE (GM124169-01) and National Institute of Health project MINOS(R01GM105404), with thanks to K. Burnett, G. Hura, M. Hammel, J. Tanamachi, and J. Tainer for the services provided through the mail-in SAXS program, which is supported by the DOE Office of Biological and Environmental Research Integrated Diffraction Analysis program DOE BER IDAT grant DE-AC02-05CH11231 and NIGMS supported ALS-ENABLE (GM124169-01) and National Institute of Health project MINOS (R01GM105404).

Further details on everything listed herein can also be found in our manuscript, which I was fortunate to work on with many of the above-listed people (*1*). My co-authors all contributed text to the manuscript that has been adapted herein.

My family as always deserves thanks for their patience and support; thank you to my sister, Sarah, and my parents, Karen and David. I write these acknowledgements with my pug Teddy curled on my lap who provides constant affirmation. To my wife, Mimi, thank you for your trust in me to restart my life to get this thesis, and for your forever-reliable love and support.

Chapter 1. Introduction to Antibodies and Nanocages

1.1 Antibody Multimerization Strategies

Antibodies are widely used therapeutic and diagnostic protein tools that are central to modern biotechnology, with the market for antibody-based technologies reaching $150 billion in 2019 (*2*). Over half of new drug therapeutics are antibodies, and hundreds of antibody therapeutics are approved to treat diseases such as cancer, viral infection, autoimmune disease, and arthritis.

Antibodies gain their incredible functionality through variable domains that are highly mutable, allowing antibodies to bind almost any molecular target, and constant domains that recruit immune cells (Fig 1.1). Most common antibodies, including those from humans and other mammalian species, comprise heavy chains (composing the full Fc and half of the Fab domain) and light chains (composing the other Fab half); both heavy and light chains comprise constant and variable domains. Antibodies are classified according to their structure and valency (i.e., how many binding domains per antibody), and each class of antibodies has a specific immunological function. For example, immunoglobulin G (IgG) antibodies are the most common circulatory antibody, with their structure characterized by two arm-like binding domains (Fabs) emanating from a conserved stem-like region (Fc); in contrast, immunoglobulin M (IgM) antibodies have five binding domains and are a first line of immunological defense. Mutations in heavy chain domains further classify the antibodies into allotypes, with corresponding

nomenclature specifying the host species and allotype, e.g. human IgG1, or mouse IgG2a.

Engineering efforts have greatly expanded beyond natural antibody formats to meet modern therapeutic, diagnostic, and research needs (Fig. 1.1). To increase binding avidity, and to enhance agonism through receptor clustering, there has been considerable interest in high valency antibody formats that present more than two antigen-binding sites (*3*, *4*). One common approach is to genetically encode flexible protein linking domains between antibody fragments of interest; the most well-known example of this technique is the single-chain variable fragment (scFv) platform, which links together two variable antibody fragments (*5*, *6*). This linkage strategy can be extended to arbitrarily long chains of scFvs or other antibody fragment domains, limited by the engineered construct's ability to be expressed and remain soluble in solution. IgM has also been engineered or derivatized, where the IgM chain is genetically combined with other antibody fragments such as IgG Fc domains (*7*). These approaches are effective at multimerizing relatively small (fewer than ten) antibody domains, but may require extensive engineering or not be structurally well-defined.

Another approach is to bind antibodies, typically IgGs, onto the surface of existing multi-component structures. IgG antibodies have been bound to the surface of inorganic materials through covalent of non-covalent interactions (*8*); in one study, it was observed that IgGs bound to inorganic gold/silica nanoparticles more effectively inhibited Wnt signaling in breast cancer cell lines compared to unbound IgG (*9*). Protein oligomers have been genetically fused to antibody fragments, and this approach has

been shown to boost antibody binding and downstream signaling (*10*). To create even larger antibody-presenting structures, antibody IgG constant domain-binding proteins have been fused to symmetric protein oligomers or nanocages (*11–15*). These structures have the potential to bind as many antibodies as there are individual protein components, and can form antibody conjugates by simply mixing the oligomer-binder protein with arbitrary IgGs. However, it is difficult to ensure full occupancy on the oligomer or nanocage surface and to prevent particle flocculation induced when multiple oligomers bind to each side of dimeric IgGs.

To my knowledge, no methods exist for creating antibody-based protein nanoparticles across multiple valencies with precisely-controlled geometry and composition that are applicable to the vast number of off-the-shelf IgG antibodies. This motivates the primary goal of my thesis, which was to design proteins that drive the assembly of arbitrary antibodies into symmetric, well-defined structures.

1.2 Nanocage Design and Functionalization

Nanocages have been successfully built out of protein building blocks with cyclic symmetry, and so C2 cyclically symmetric IgG antibodies could also be built into nanocages. IgGs are a type protein with “cyclic symmetry,” defined as the ability to rotate the protein around a symmetry axis in a way that recapitulates the starting structure (*16*). The type of cyclic symmetry is determined by the number of rotations that match the starting structure during a full 360° rotation. For example, a cyclic 2 or C2 symmetric protein can be rotated twice (180° and 360°), and a C3 protein can be

rotated three times (120°, 240°, 360°) with each rotation creating an identical structure to the input. Larger protein structures that combine multiple cyclic symmetry axes can create point group symmetries if the cyclic symmetry axes all intersect in the center of the larger structure. For instance, an I52 icosahedral assembly is built by bringing together a C5 pentamer and a C2 dimer that align to the icosahedral five- and two-fold symmetry axes, respectively. As antibodies are C2 symmetric proteins, nanocages can be built using antibodies as core structural components aligning to any point group symmetry's C2 axes. To hold the antibodies along the two-fold axes of dihedral or polyhedral architectures, a second cage-forming component needed to be designed along a second nanocage symmetry axis.

To design proteins that assemble into nanocages, cyclically symmetric protein building blocks must be brought together to design larger nanocage architectures. Two common strategies for designing protein nanocages are computationally docking (*17*, *18*) or fusing (*19*–*21*) cyclically symmetric proteins (Fig. 1.2).

Protein docking refers to the computational alignment of cyclic oligomers near each other in three-dimensional space, and this new structure is typically stabilized via the design of a *de novo* non-covalent protein-protein interface design. During the docking step, many docked conformations are formed by varying the cyclic oligomers' relative rotational and translational positions along their symmetry axes. Structures in which the oligomers' backbones fit best with each other are determined by calculating the contacting surface area, shape complementarity, and other similar interface metrics. Researchers have successfully employed this docking strategy to design nanocage

vaccines (*17*), cargo containers (*18*), or signaling super-agonists (*22*). However, docked cage design works best when both cage-forming components are redesigned, and to my knowledge there are no current reports of successful cage formation arising from one-sided interface design. Therefore, this approach would not be adaptable to the vast library of existing off-the-shelf antibody IgGs.

Nanocage design via protein fusion has more promise for creating nanocages that incorporate antibodies as key structural and functional components. Fusion has been previously accomplished by designing a linking alpha-helical motif between two chains of cyclic oligomers. This approach was used to create a single-component I532 icosahedral structure, where the monomeric component has separate C5, C3, and C2 interfaces (*21*). Another more recent fusion-based approach for designing nanocages splices protein chains directly together without the need for adding a new helical structure. In this approach (named “WORMS”), alpha helical protein motifs are aligned *in silico* (i.e., computationally overlapping the helices) and the fusion occurs directly between protein chains to create a new, continuous alpha helix. After fusion, WORMS checks that the new orientation of the oligomeric interfaces matches the desired geometry. This approach was successfully used to design dihedral and icosahedral nanocages, with some designs incorporating functional ankyrin loop-containing domains (*19*, *20*). WORMS is an excellent method for designing antibody nanocages by fusing alpha helical domains of antibody-binding proteins to existing cyclic oligomers in the orientations required to form nanocages, as this approach wouldn’t require designing (i.e., mutating) any part of the antibody.

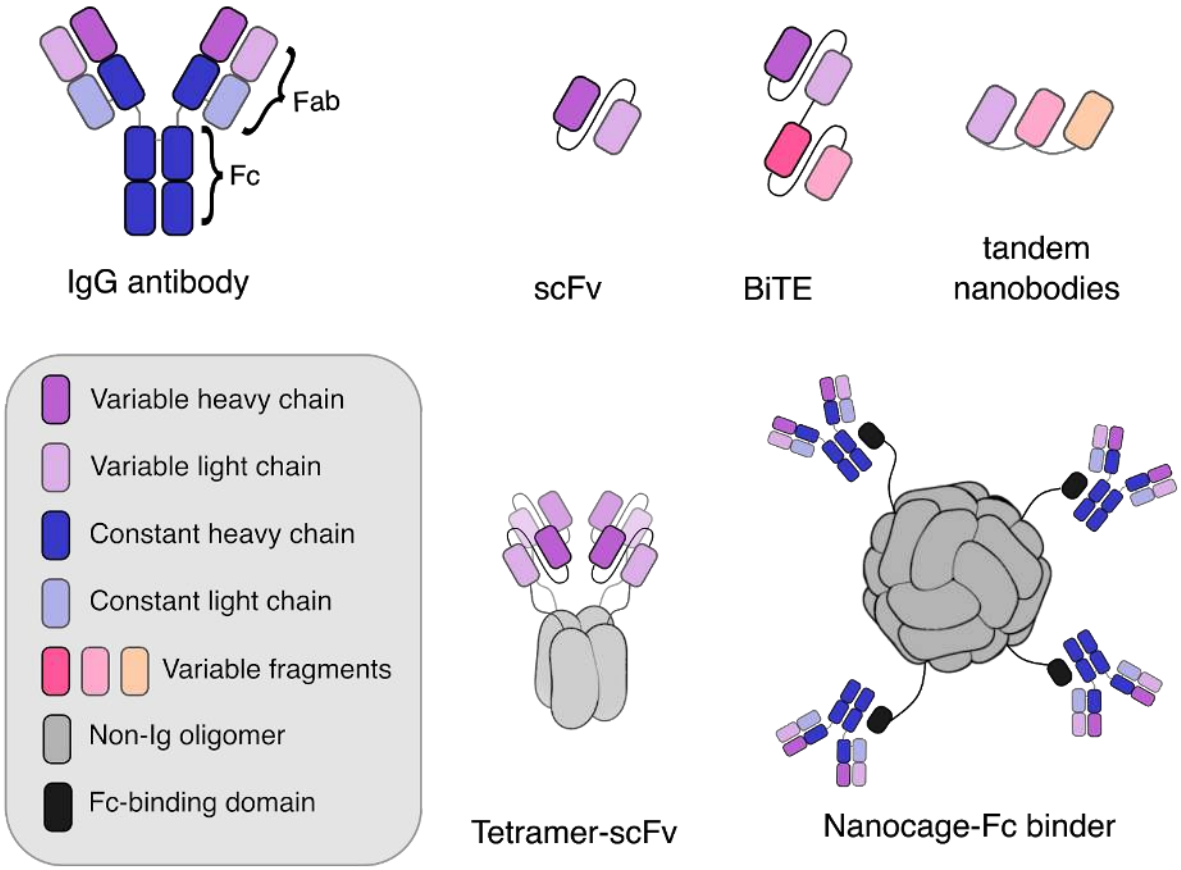

Figure 1.1 Antibody multimerization strategies. Top left, IgG antibody structure colored by domain. Top right, multimeric fragments can be built by chaining together short chain variable fragments (scFv) to create bispecific T cell engagers (BiTEs) or by fusing variable fragment domains (*4*). Bottom right, protein oligomers that form small oligomers or nanocages can be fused to scFvs or Fc-binding domains to create larger multimeric antibody structures (*10*–*12*). Bottom left, legend.

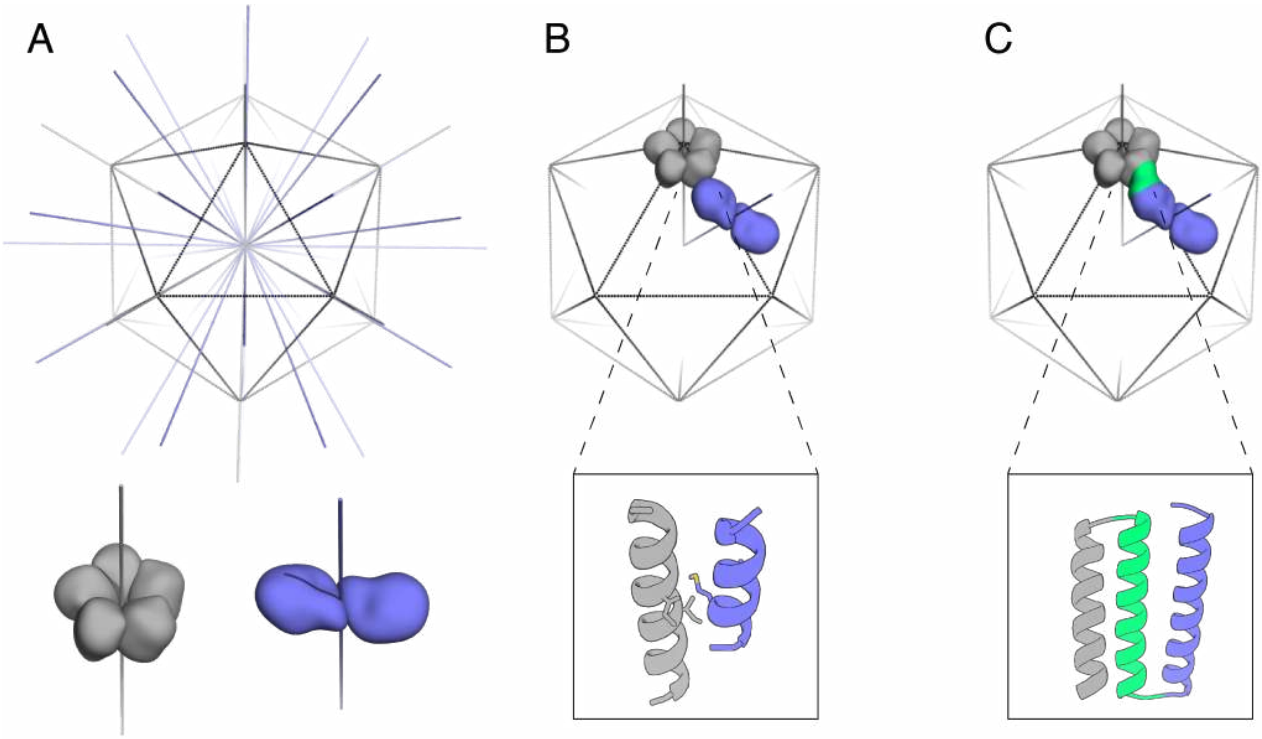

Figure 1.2 Nanocage design strategies. A, To design a protein that forms along the symmetry axes of a polyhedron such as an icosahedron, cyclic protein oligomers must be placed along the polyhedra's symmetry axes (grey, C5 protein and symmetry axes along the black I52 wireframe; purple, C2 protein and axes). **B,** C5 and C2 proteins docked together to form an I52 icosahedral assembly, with a non-covalent interface designed between proteins to stabilize the assembly. **C,** C5 and C2 proteins fused together to form an I52 icosahedral assembly, with a green linking protein (which can be added as a fragment or formed from overlapping existing helices) showing the fusion site.

Chapter 2. Computational Design of Antibody Nanocages

2.1 Helical Fusion to Design Antibody Nanocage Backbones

The first aim of my thesis project was to antibody-binding, nanocage-forming protein that precisely arranges IgG dimers along the two-fold symmetry axes of a target architecture. I used WORMS to rigidly fuse together three types of “building block” proteins: antibody Fc-binding proteins, monomeric helical connectors, and cyclic oligomers; each building block plays a key role in the final fusion protein. The Fc-binder forms the first nanocage interface between the antibody and the nanocage-forming design, the cyclic homo-oligomer forms the second nanocage interface between designed protein chains, and the connector links the two interfaces together in the correct orientation for nanocage formation. The designed cage-forming protein is thus a cyclic oligomer terminating in antibody-binding domains that bind dimeric (C2) IgG antibodies at the orientations required for the proper formation of antibody nanocages (hereafter AbCs, for Antibody Cages). Fig. 2.1 provides an overview of the full design process, which is further detailed in this chapter.

Key to the success of this fusion approach is a sufficiently large set of building blocks to fuse, and possible fusion sites per building block, to meet the rather stringent geometric criteria (described below) required to form the desired symmetric architecture. Two different Fc-binder building blocks were provided as inputs. The first was the D domain of protein A, which binds to the Fc domain of the IgG constant region, with minimal Fab domain binding compared to other protein A domains (PDB ID 1DEE

for protein A; PDB ID 1L6X for Fc) (*23*, *24*). A second Fc-binding building block was designed by grafting the protein A interface residues onto a previously designed helical repeat protein (Fig. 2.2). Grafted binder designs were assessed via yeast display and biolayer interferometry; please see the following reference for a full description of the helical grafting design and analysis methods as provided by Franziska Seeger (*1*), adapting published techniques for design and yeast display (*24*–*26*).

The final building block library consisted of these 2 Fc-binding proteins (*23*), 42 *de novo* designed helical repeat connectors (*27*), and between 1-3 cyclic homo-oligomers depending on geometry (2 C2s, 3 C3s, 1 C4, and 1 C5) (*28*, *29*). An average of roughly 150 residues were available for fusion per protein building block, avoiding fusions at all positions at the Fc or homo-oligomer protein interface. This creates an order of 10^7 possible tripartite (i.e., Fc-binder/connector/homo-oligomer) fusions. For each of these tripartite fusions, the rigid body transform between the internal homo-oligomeric interface and the Fc-binding interface is determined by the shapes of each of its three building blocks and the locations and geometry of the "junctions" that link them into a single subunit.

The WORMS computational protocol was used to rapidly sample all possible fusions from our building block library to identify those with the net rigid body transforms required to generate dihedral, tetrahedral, octahedral, and icosahedral AbCs (*19*, *20*). To describe the final nanocage architectures, a naming convention is used which summarizes the point group symmetry and the cyclic symmetries of the building blocks (*18*). For example, a T32 assembly has tetrahedral point group symmetry and is built

out of a C3 cyclic symmetric designed antibody-binding oligomer, and the C2 cyclic symmetric antibody Fc. While the antibody dimer aligns along the two-fold axis in all architectures, the designed component is a second homodimer in D2 dihedral structures; a homotrimer in T32 tetrahedral structures, O32 octahedral structures, and I32 icosahedral structures; a homotetramer in O42 octahedral structures; and a homopentamer in I52 icosahedral structures.

To make the fusions, WORMS first aligns the model of the Fc and Fc-binder protein along the C2 axis of the specified architecture (Fig. 2.1a-b). The Fc-binder is then fused to a connector, which is in turn fused to a homo-oligomer. Rigid helical fusions are made by superimposing residues in alpha helical secondary structure from each building block; in the resulting fused structure one building block chain ends and the other begins at the fusion point, forming a new, continuous alpha helix (Fig. 2.1c). To drive formation of the desired nanocage architecture, fusions are made such that the antibody two-fold axis and the symmetry axis of the homo-oligomer intersect at specified angles at the center of the architecture (Fig. 2.1d). To generate D2 dihedral, T32 tetrahedral, O32 or O42 octahedral, and I32 or I52 icosahedral nanocages, the required intersection angles are 90.0°, 54.7°, 35.3°, 45.0°, 20.9°, and 31.7°, respectively (*16*). We allowed angular and distance deviations from the ideal architecture of at most 5.7° and 0.5 Å, respectively. Candidate fusion models were further filtered based on the number of contacts around the fusion junction (to gauge structural rigidity) and clashes between backbone atoms. Information about how to install and run the helical fusion methods can be found at https://zenodo.org/record/444120. Building block .pdb files and

specific methods developed to create antibody cage backbones via this fusion approach can be found at https://zenodo.org/record/4599680.

2.2 Post-fusion Sidechain Design

Post-fusion .pdb files were manually filtered to ensure that the N-termini of the Fc domains are facing outwards from the cage, so that the Fabs of an IgG would be external to the cage surface. The amino acid identities and conformations around the newly formed building block junction were optimized using the SymPackRotamersMover in Rosetta to maintain the rigid fusion geometry required for assembly. I focused on re-designing residues at and around the fusion junctions (*30*), especially where polar residues from the original building block now faced the protein core, or nonpolar residues were on the surface, while trying to maintain as many of the native residues as possible. I also redesigned any clashes (i.e., proteins overlapping in space in unrealistic ways) that were introduced during the fusion process by mutating clashing residues to smaller sidechains. Index residue selectors were used to prevent design at Fc residue positions. (Fig. 2.1e). Following sequence design, we selected for experimental characterization six D2 dihedral, eleven T32 tetrahedral, four O32 octahedral, two O42 octahedral, fourteen I32 icosahedral, and eleven I52 icosahedral designs predicted to form AbCs (Fig. 2.1f). All 48 design .pdb models can be found, along with examples of the design protocol, at https://zenodo.org/record/4599680.

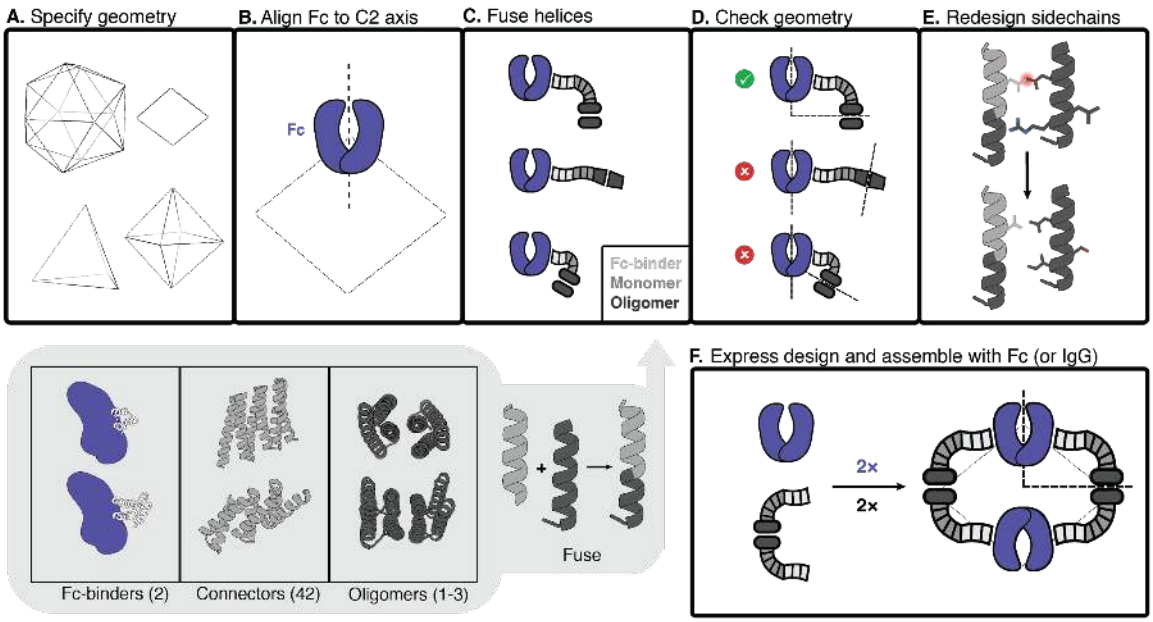

Figure 2.1. Antibody nanocage (AbC) design. A, Polyhedral geometry is specified. Clockwise from top left: icosahedral, dihedral, octahedral, and tetrahedral geometries are shown. **B,** An antibody Fc model from hIgG1 is aligned to one of the C2 axes (in this case, a D2 dihedron is shown). **C,** Antibody Fc-binders are fused to helical repeat connectors that are then fused to the monomeric subunit of helical cyclic oligomers. All combinations of building blocks and building block junctions are sampled (below inset, grey). **D,** Tripartite fusions are checked to ensure successful alignment of the C2 Fc symmetry axes with that of the polyhedral architecture (in the case of the D2 symmetry shown here, the C2 axes must intersect at a 90° angle). **E,** Fusions that pass the geometric criteria move forward with sidechain redesign, where e.g. amino acids are optimized to ensure that core-packing residues are nonpolar and solvent-exposed residues are polar. **F,** Designed AbC-forming oligomers are bacterially expressed, purified, and assembled with antibody Fc or IgG.

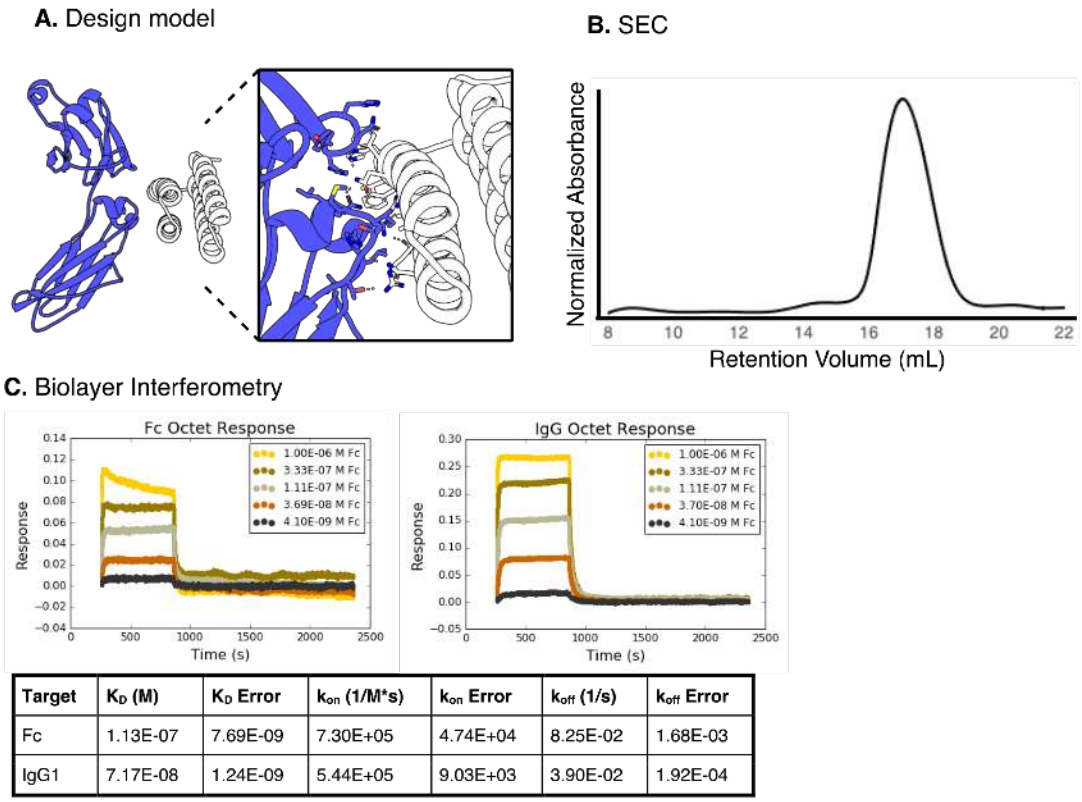

Target	K_D (M)	K_D Error	k_{on} (1/M*s)	k_{on} Error	k_{off} (1/s)	k_{off} Error
Fc	1.13E-07	7.69E-09	7.30E+05	4.74E+04	8.25E-02	1.68E-03
IgG1	7.17E-08	1.24E-09	5.44E+05	9.03E+03	3.90E-02	1.92E-04

Figure 2.2. Design of an Fc-binding repeat protein. A, Model of the helical repeat protein DHR79 (*27*) docked against antibody Fc (PDB ID: 1L6X). Residues from protein A (PDB ID: 1DEE) are grafted at the interface between the Fc and the helical repeat protein. **B,** Superdex 200 SEC trace of the Fc-binding helical repeat monomer. **C,** Biolayer interferometry (BLI) of the Fc-binding helical repeat design with Fc (left) or with hIgG1 (right), with summary statistics (below).

Chapter 3. Structural Confirmation of Antibody Nanocages

3.1 Protein Expression and Oligomer Characterization

Codon-optimized genes encoding designed protein sequences, appended with a C-terminal glycine/serine linker and a 6× histidine tag, were synthesized and inserted into a pet29b+ vector (ordered from Integrated DNA Technologies). Plasmids were transformed into Lemo21 (DE3) *E. coli* using a 15-second, 37 °C heat shock protocol. Successfully-transformed cells were separated by plating onto kanamycin agar plates, as the pet29b+ vector also encoded a kanamycin-resistant gene. Transformed cells were added to auto-induction expression media (6 g tryptone, 12 g yeast extract, 10 mL 50×M, 10 mL 50x5052, 1 mL 1M $MgSO_4$, 100 µL Studier Trace metals, 50 µg kanamycin antibiotic, brought to a final volume of 500 mL using filtered water) and incubated for 16 hours at 37 °C and 200 rpm shaking (*31*).

Cells were pelleted via centrifugation at 4000 rpm, and lysis buffer (150 mM NaCl, 25 mM Tris-HCl, pH 8.0, added protease inhibitor and DNAse) was added to resuspend the separated cell pellets. Sonication was used to lyse the cells at 85% amplitude, with 15 second on/off cycles for a total of 2 minutes of sonication time. Soluble material was separated by centrifugation at 16000×g. Immobilized metal affinity chromatography (IMAC) was used to separate out the His-tagged protein: nickel-nitrilotriacetic acid (Ni-NTA) resin was equilibrated with binding buffer (20 mM Tris, 300 mM NaCl, 30 mM imidazole, pH 8.0), soluble lysate was poured over the columns, columns were washed with 20 column volumes (CVs) of binding buffer, and

eluted with 5 CVs of elution buffer (20 mM Tris, 300 mM NaCl, 500 mM imidazole, pH 8.0). IMAC elutions were concentrated to approximately 1 mL using 10K MWCO spin concentrators, filtered through a 0.22 μM filter, and run over SEC as a final purification step (SEC running buffer: 150 mM NaCl, 25 mM Tris-HCl, pH 8.0). Across all geometries, 35 out of 48 AbC-forming designs had a peak on SEC that roughly corresponded to the expected size of the design model (Fig. 3.1, Table 3.1).

3.2 Structural Characterization of AbCs using SEC, EM and SAXS

Designs were then combined with human IgG1 Fc, and the assemblies were purified via SEC. Eight of these AbC-forming designs readily self-assembled after mixing with human IgG1 Fc fragment into a species that eluted as a monodisperse peak at a volume consistent with the target nanocage molecular size (Fig. 3.2a-b; 3 D2 dihedral, 2 T32 tetrahedral, 1 O42 octahedral, and 2 I52 icosahedral AbCs). Designs were incubated with Fc for at least 30 minutes at 4 °C. For the i52.6 design, adding 100 mM L-arginine to the assembly buffer prevented aggregation after combining with Fc (*32*); all other designs readily self-assembled in Tris-buffered saline (TBS). Of these eight AbC-forming designs, all designs expressed well, with SEC-purified protein yields between 50-100 mg protein/L of bacterial culture. After combining with Fc, at least 90% of the protein injected on SEC is recovered in the assembly (left-most) peak (Fig. 3.2b). SEC peaks for the T32 and O42 designs were somewhat broader than other designs, spanning 3-4 mL in retention volume, as observed in previous nanocage design efforts (*18*). The I52 designs eluted in the void volume, consistent with their predicted

diameters. Most other designs still bound Fc, as evidenced by SEC or by visibly precipitating with Fc after combination, but did not form monodisperse nanocages by SEC (Table 3.1), perhaps because of deviations from the target fusion geometry. Cryo-EM of o42.1 and i52.3 AbCs, and negative stain-EM (NS-EM) of the other six AbCs, showed monodisperse particle formation with individual cages, and 2D class averages resemble the design models (Fig. 3.2c; Tables 3.2, 3.3).

AbCs also formed when assembled with full IgG antibodies (containing both Fc and Fab domains) again generating monodisperse nanocages as shown by SEC and NS-EM (Fig. 3.2d-e; Tables 3.2, 3.3); here, the o42.1 design with IgG reproducibly elutes in the void due to the increased diameter from the added Fab domains. The data in Figure 3.2d-e shows AbCs formed with the α-DR5 antibody AMG-655 (*32*) for the following designs: d2.3, d2.4, d2.7, t32.4, t32.8, o42.1, and i52.3. The data for the i52.6 design shown in Figure 3.2d-e is from AbCs formed with the hIgG1 antibody mpe8 (*33*); this was simply due to limited AMG-655 availability at the time of the experiment and not a reflection on i52.6/AMG-655 assembly competency. There is considerably more evidence of flexibility in the electron micrographs of the IgG-AbCs than the Fc-AbCs, as expected given the flexibility of the Fc-Fab hinge. In all cases, 2D class averages obtained from the NS-EM data of AbCs made with intact IgG resolved density corresponding to the Fc and the design portion of the assembly (Fig. 3.2e).

Single-particle NS-EM and cryo-EM reconstructed 3D maps of the AbCs formed with Fc are in close agreement with the computational design models (Fig. 3.3). Negative-stain EM reconstructions for the dihedral (d2.3, d2.4, d2.7), tetrahedral (t32.4,

t32.8), and one of the icosahedral (i52.6) nanocages clearly show dimeric “U”-shaped Fcs and longer designed protein regions that fit together as computationally designed. A single-particle cryo-EM reconstruction for the o42.1 design with Fc has clear density for the six designed tetramers sitting at the C4 vertices, which twist along the edges of the octahedral architecture to bind twelve dimeric Fcs, leaving the eight C3 faces unoccupied. The 3D density map for o42.1 with Fc suggests that the particle is flexing outwards compared to the design model. Cryo-EM density for i52.3 with Fc likewise recapitulates the 20-faced shape of a regular icosahedron, with 12 designed pentamers protruding at the C5 vertices (due to the longer length of the C5 building block compared to the monomer or Fc-binder), binding to 30 dimeric Fcs at the center of the edge, with 20 unoccupied C3 faces. Asymmetric cryoEM reconstructions of o42.1 with Fc and i52.3 with Fc had similar overall features to their respective symmetrized maps (Fig. 3.4). Full methods details for EM grid preparation and data collection as provided by Ha Dang and David Veesler can be found at our paper describing this work (*1*), using previously published EM analysis techniques (*34*–*37*).

We further characterized the eight promising Fc-AbCs by small-angle X-ray scattering (SAXS). Fc AbCs were purified for SAXS analysis via SEC into 150 mM NaCl and 25 mM Tris-HCl buffer at pH 8.0. Fractions corresponding to the Fc AbC peak after SEC were combined and glycerol was added at 2% final concentration. Samples were concentrated to between 1-3 mg/mL using a 10K molecular weight cut-off (MWCO) benchtop spin concentrator. The flow-through was used as a blank for buffer subtraction during SAXS analysis. Proteins were then passed through a 0.22 μm syringe filter

(Millipore). These proteins and buffer blanks were shipped to the SIBYLS High Throughput SAXS Advanced Light Source in Berkeley, California to obtain scattering data (*38*). Scattering traces were fit to theoretical models using the FOXS server (*39*). ScÅtter3 was used for radius of gyration (R_g), d_{mas}, q_{max}, and pair distance distribution (P(r)) analyses (https://bl1231.als.lbl.gov/scatter/). For the P(r) distributions, the Kullback-Leibler divergence (D) of the experimental data from the design model was calculated; Shannon sampling was used to determine the number of points from which to calculate D (*40*).

SAXS spectra, P(r) distributions, R_g values were close to design models for d2.4, d2.7, t32.4, o42.1, i52.3, and i52.6 Fc-AbCs (Fig. 3.5, Table 3.4) (*38*, *39*). The agreement to the SAXS data for the d2.3 and t32.8 design models was somewhat less good (higher R_g values, and deviations in the SAXS Guinier (low-q) region and P(r) distributions from those computed from the design model) potentially due to alternate particle states, flexibility, and (or) particle aggregation during data collection.

3.3 Nanocage Stability

We next assessed the stability of AbCs using dynamic light scattering (DLS) and SDS-PAGE. Fc AbC samples were prepared for stability analysis by mixing equimolar amounts of each AbC-forming design component with hIgG1 Fc domain. These were purified using SEC using a Superose 6 column, following similar techniques as described above, into tris buffered saline (150 mM NaCl, 25 mM Tris-HCl pH 8.0) with 50 mM L-arginine (from a 1 M L-arginine pH 8.0); L-arginine was added to all designs

as it had been observed to reduce hydrophobic association for the i52.6 AbCs. After SEC, the fractions corresponding to the AbC (left-most peak) were pooled. These were incubated at room temperature and analyzed once per week for up to five weeks post-SEC via DLS and SDS-PAGE. Dynamic light scattering measurements (DLS) were performed using the default Sizing and Polydispersity method on the UNcle (Unchained Labs). 8.8 µL of AbCs were pipetted into the provided glass cuvettes. DLS measurements were run in triplicate at 25 °C with an incubation time of 1 second; results were averaged across runs and plotted using matplotlib. DLS readings remained constant over a period of 4 weeks for all designs when incubated at room temperature, with the exception of i52.6 which showed some broadening of the hydrodynamic radius after 2-3 weeks (Fig. 3.6a). DLS peak statistics can be found at https://zenodo.org/record/4670723.

Fc AbCs also did not show any degradation according to SDS gel electrophoresis (Fig. 3.6b). To prepare samples for SDS-PAGE, 10 µL of Fc AbCs were diluted to approximately 0.1 mg/mL and prepared for SDS by mixing with 2 µL of 6× loading dye (197 mM Trs-HCl, pH 6.8; 70% glycerol; 6.3% SDS; 0.03% bromephenol blue); these were then heated for 5-10 minutes at 95°C and loaded into the wells of a Tris-Glycine gel (Bio-Rad, catalogue #5678125). SDS running buffer was prepared to a final concentration of 5 mM Tris, 192 mM glycine, 0.1% SDS, pH 8.3. 2-5 µL of ladder was also added (BioRad 161-0377 or 161-0374). The gel was run for 25-30 minutes at 180-200 V or until the dye reached near the bottom of the gel. Gels were stained with Coomassie Brilliant Blue dye using the Genscript eStain protein staining system.

We investigated whether AbCs formed with one Fc-fusion or IgG would exchange when incubated with excess Fc; this is relevant to future *in vivo* applications of the AbCs where they would be in the presence of high concentration serum IgG. GFP-Fc was mixed with o42.1 tetramer; a pre-mixed ratio of RFP-Fc and GFP-Fc (at a 25:1 molar ratio) was separately combined with o42.1 tetramer as a positive control meant to mimic 100% exchange, as the GFP-Fc o42.1 AbC would be mixed with 25-fold excess RFP-Fc (Fig. 3.7a). Fc-GFP o42.1 and 25:1 Fc-RFP:GFP o42.1 were purified via a Superose 6 SEC column into TBS with 50 mM L-arginine. Fc-GFP o42.1 was then incubated with 25-fold excess Fc-RFP and separated using an autosampler; the autosampler was necessary to control injection volume (Cytiva ALIAS autosampler; Fig. 3.7b). Time points were taken at 5 minutes, 2 hours, 4 hours, and 24 hours after mixing and incubation at 25 °C. Controls were GFP-Fc o42.1 without added Fc-RFP, Fc-RFP without AbC, and the 25:1 “pre-exchanged” control. 100 µL from each SEC peak fraction were then transferred to a 96-well fluorescence plate (Corning, black polystyrene). To measure GFP signal, excitation and emission wavelengths were set to 485/510 (respectively); for RFP signal, excitation and emission wavelengths were set to 558/605 (Neo2 Microplate Reader, BioTek). Although the RFP-Fc signal increased slightly in the cage fraction (Fig. 3.7c-d), the GFP-Fc signal was very close to that of the o42.1 GFP-Fc control, suggesting little exchange of the Fc-containing component out of the cage. Statistics for all stability experiments can be found at https://zenodo.org/record/4670723. Encouraged by these stability results, the project moved to investigating the biological impact of the AbCs.

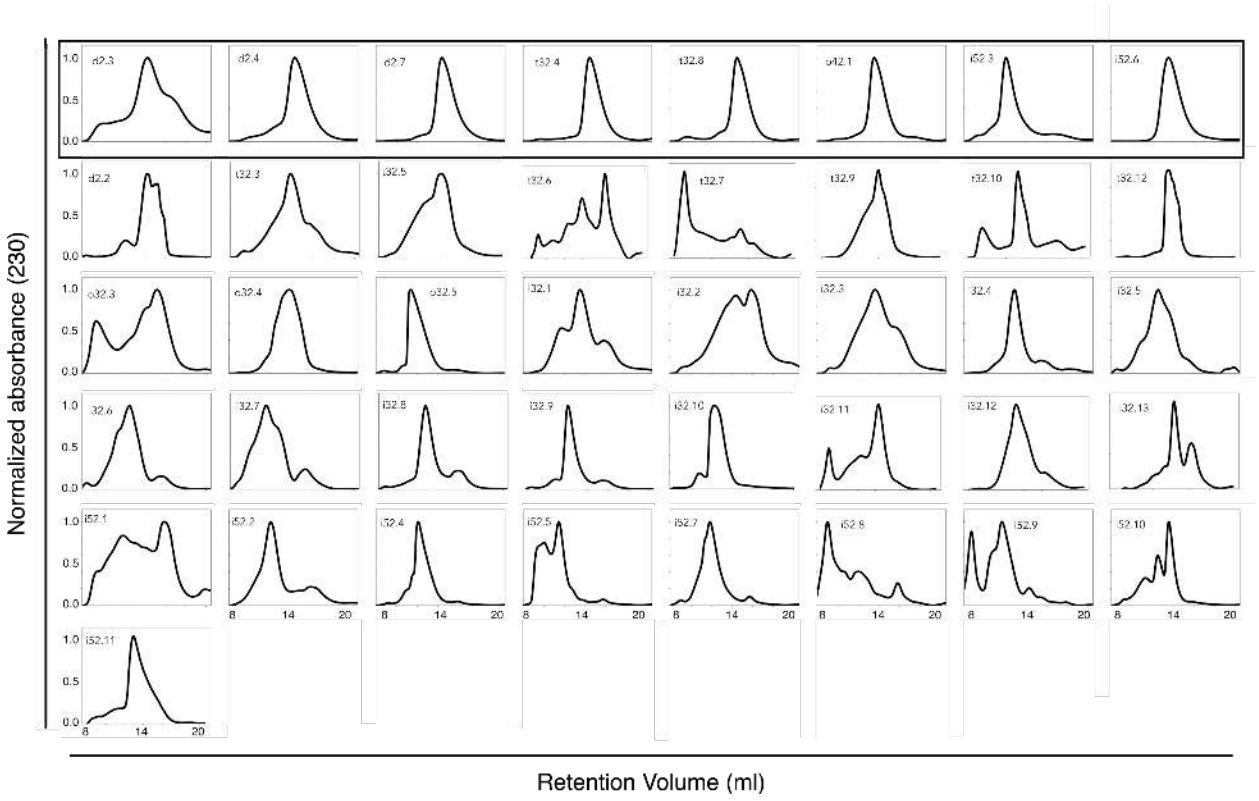

Figure 3.1 SEC of soluble designs. First row: SEC profiles of all soluble AbC-forming designs run over a Superdex 200 column. Bottom rows: all other soluble designs that did not form nanocages when mixed with antibodies. Several designs appear to still form oligomers at the expected size, but these may not have formed at the right orientation to lead to successful nanocage formation. The X-axis for each graph is retention volume, and the Y-axis is normalized A230 absorbance.

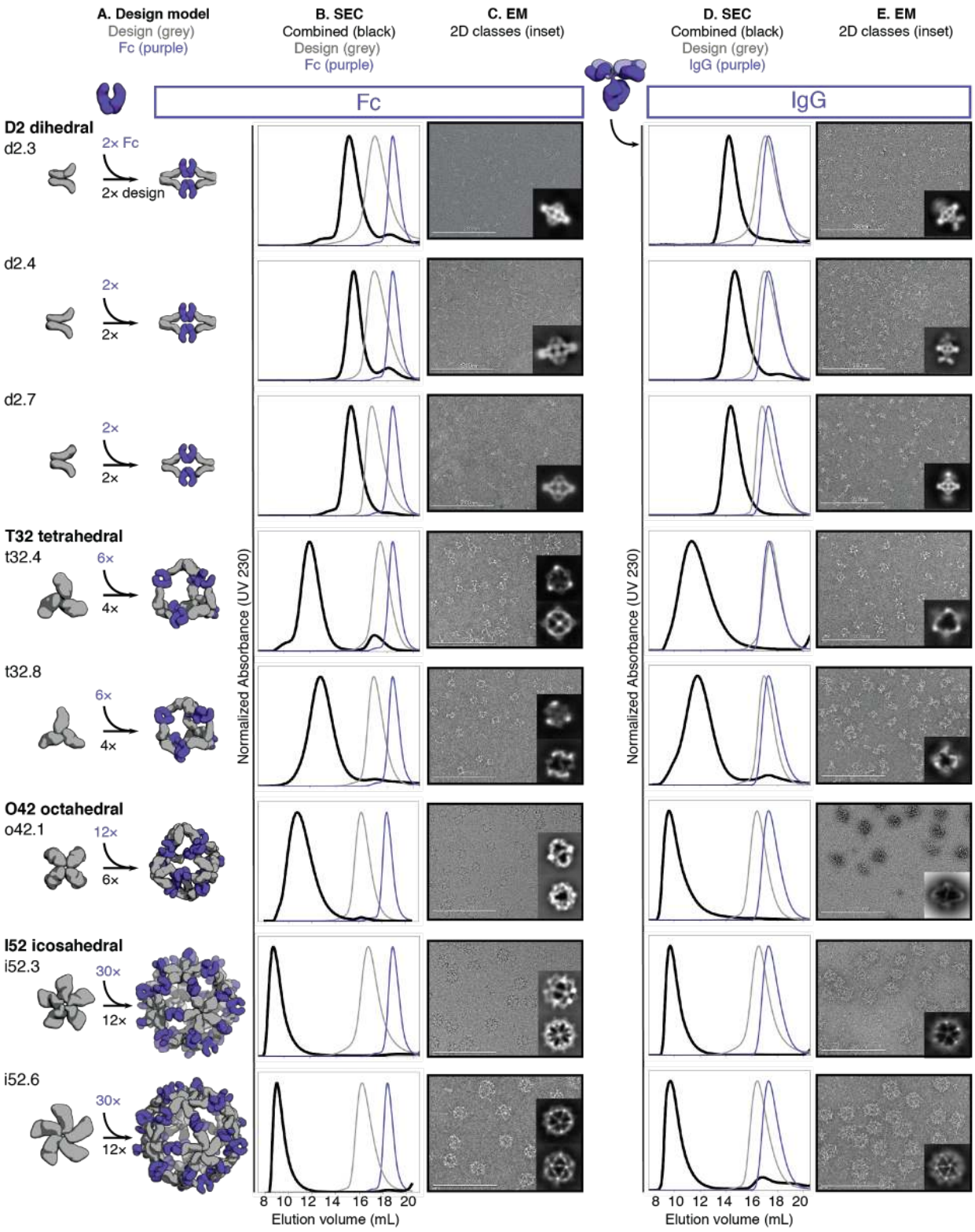
A. Design model
Design (grey)
Fc (purple)
B. SEC
Combined (black)
Design (grey)
Fc (purple)
C. EM
2D classes (inset)
D. SEC
Combined (black)
Design (grey)
IgG (purple)
E. EM
2D classes (inset)
Fc
IgG
D2 dihedral
d2.3
2× Fc
2× design
d2.4
2×
2×
d2.7
2×
2×
T32 tetrahedral
t32.4
6×
4×
t32.8
6×
4×
O42 octahedral
o42.1
12×
6×
I52 icosahedral
i52.3
30×
12×
i52.6
30×
12×
Normalized Absorbance (UV 230)
Normalized Absorbance (UV 230)
8 10 12 14 16 18 20
Elution volume (mL)
8 10 12 14 16 18 20
Elution volume (mL)

Figure 3.2 SEC and EM of working designs. A, Design models, with antibody Fc (purple) and designed AbC-forming oligomers (grey). **B,** Overlay of representative SEC traces of assembly formed by mixing design and Fc (black) with those of the single components in grey (design) or purple (Fc). **C,** EM images with reference-free 2D class averages in inset; all data is from negative-stain EM with the exception of designs o42.1 and i52.3 (cryo-EM). **D-E,** SEC (**D)** and NS-EM representative micrographs with reference-free 2D class averages (**E**) of the same designed antibody cages assembled with full human IgG1 (with the 2 Fab regions intact). In all EM cases shown in **C** and **E**, assemblies were first purified via SEC, and the fractions corresponding to the left-most peak were pooled and used for imaging; this was mainly done to remove any excess of either design or Ig component.

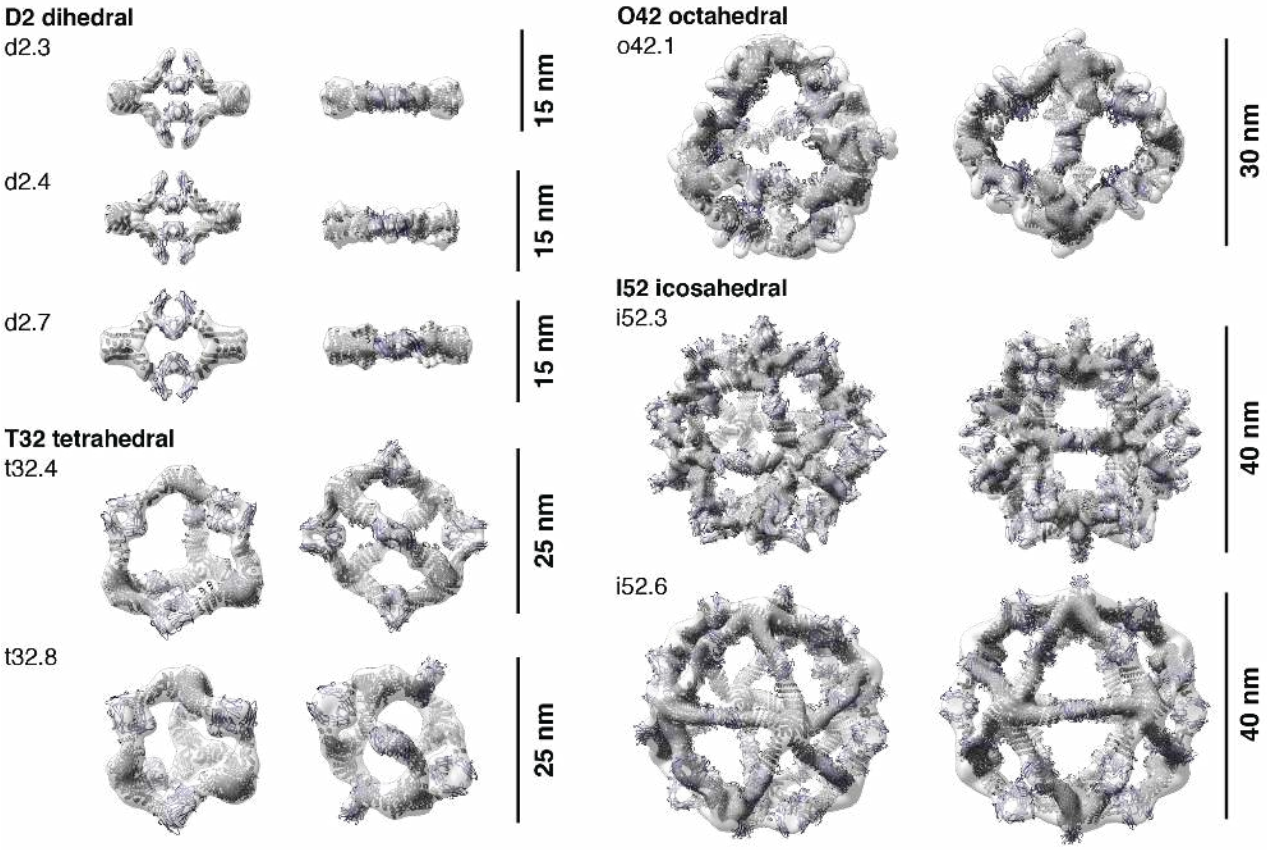

Figure 3.3. Computational design models (cartoon representation) of each AbC are fit into the experimentally-determined 3D density from EM. Each nanocage is viewed along an unoccupied symmetry axis (left), and after rotation to look down one of the C2 axes of symmetry occupied by the Fc (right). 3D reconstructions from o42.1 and i52.3 are from cryo-EM analysis; all others, from NS-EM.

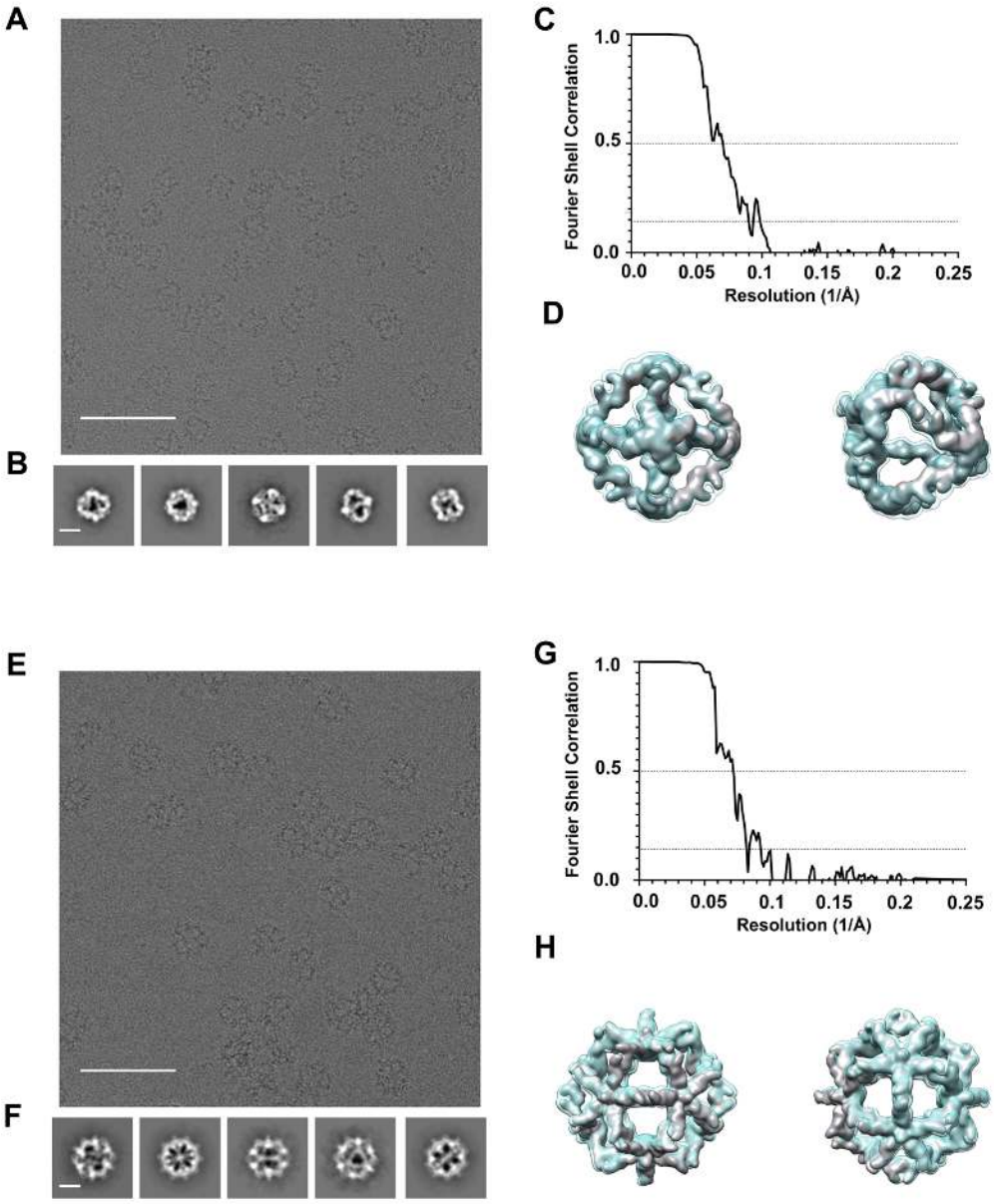

Figure 3.4 Cryo-EM data for o42.1-Fc and i52.3-Fc. A, Representative cryo EM micrograph of o42.1 Fc. Scale bar: 100 Å. **B,** Reference-free 2D class averages of o42.1-Fc. Scale bar, 200 Å. **C,** Gold-standard Fourier shell correlation curves for the o42.1 Fc map with O symmetry applied. The dotted lines indicate the 0.143 and 0.5 thresholds. **D,** Two views of the o42.1 Fc cryo-EM map reconstructed with no symmetry (transparent cyan) superimposed on the o42.1 Fc cryo-EM map with O symmetry applied (solid gray). **E,** Representative micrograph of i52.3 Fc. Scale bar: 100Å. **F,** Reference-free 2D class averages of i52.3 Fc. Scale bar, 200 Å. **G,** Gold-standard Fourier shell correlation curves for the i52.3 Fc map with I symmetry applied. The dotted lines indicate the 0.143 and 0.5 thresholds. **H,** Two views of the i52.3 Fc cryo-EM map reconstructed with no symmetry (transparent cyan) superimposed on the i52.3 Fc cryo-EM map with I symmetry applied (solid gray).

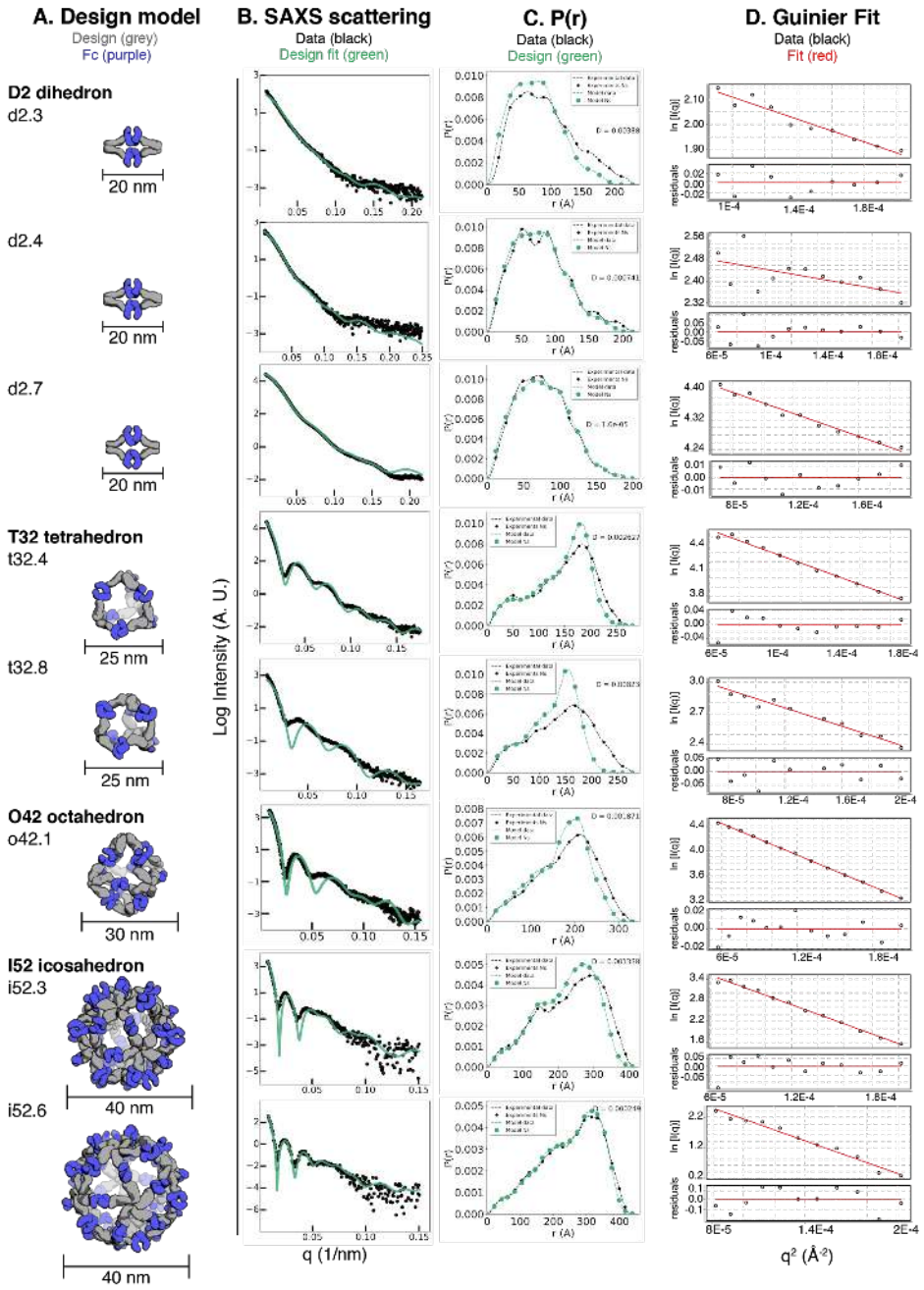

Figure 3.5 SAXS of working designs. A, Design models show designed Fc-binding oligomers in grey and antibody Fc in purple. **B,** Small angle X-ray scattering (SAXS) curve fit for all designs with Fc; Black dots represent experimentally-determined data, and the green lines are calculated from the design models, with the FOXS server (*18*) used to perform the curve fitting. **C,** Pair distance distribution functions (P(r) curves) for experimental data (black) compared to theoretical distribution functions from the design models (green). Kullback-Leibler divergences (D) of the experimental data from the models are reported. **D,** Guinier fits (top) for data up to ~2E-4 q^2 with residual error (bottom). ScÅtter3 was used to perform the P(r) and Guinier analyses.

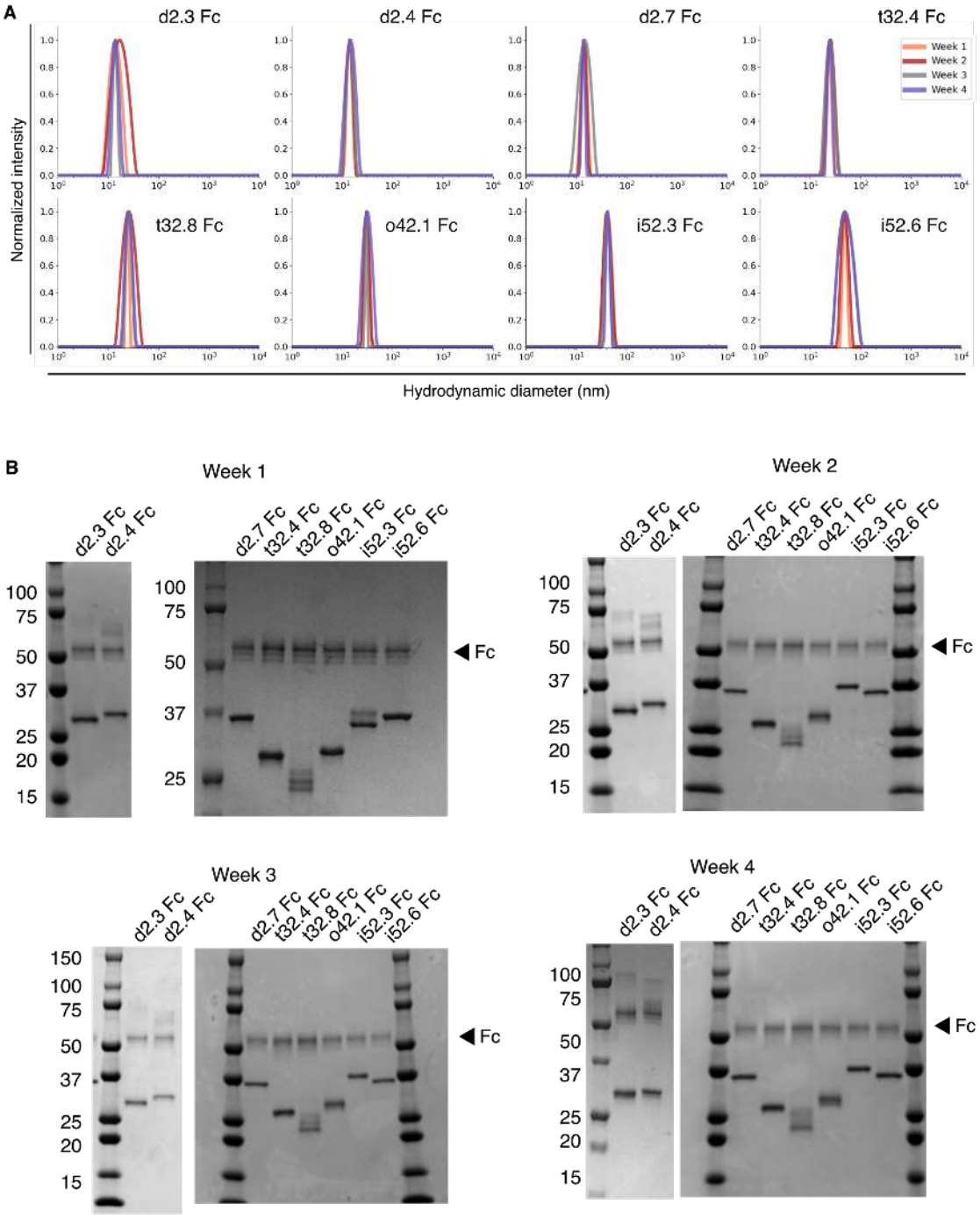

Figure 3.6 Stability testing via DLS and SDS-PAGE. A, Dynamic light scattering (DLS) of Fc AbCs, incubated at 25 °C, and measured once per week. Traces are an average of 4 measurements each. See https://zenodo.org/record/4670723 for DLS statistics. **B,** SDS-PAGE analysis of Fc AbCs (without reducing agent), incubated at 25 °C, and measured once per week. Molecular mass standards were run on outer lanes with masses (KDa) labeled.

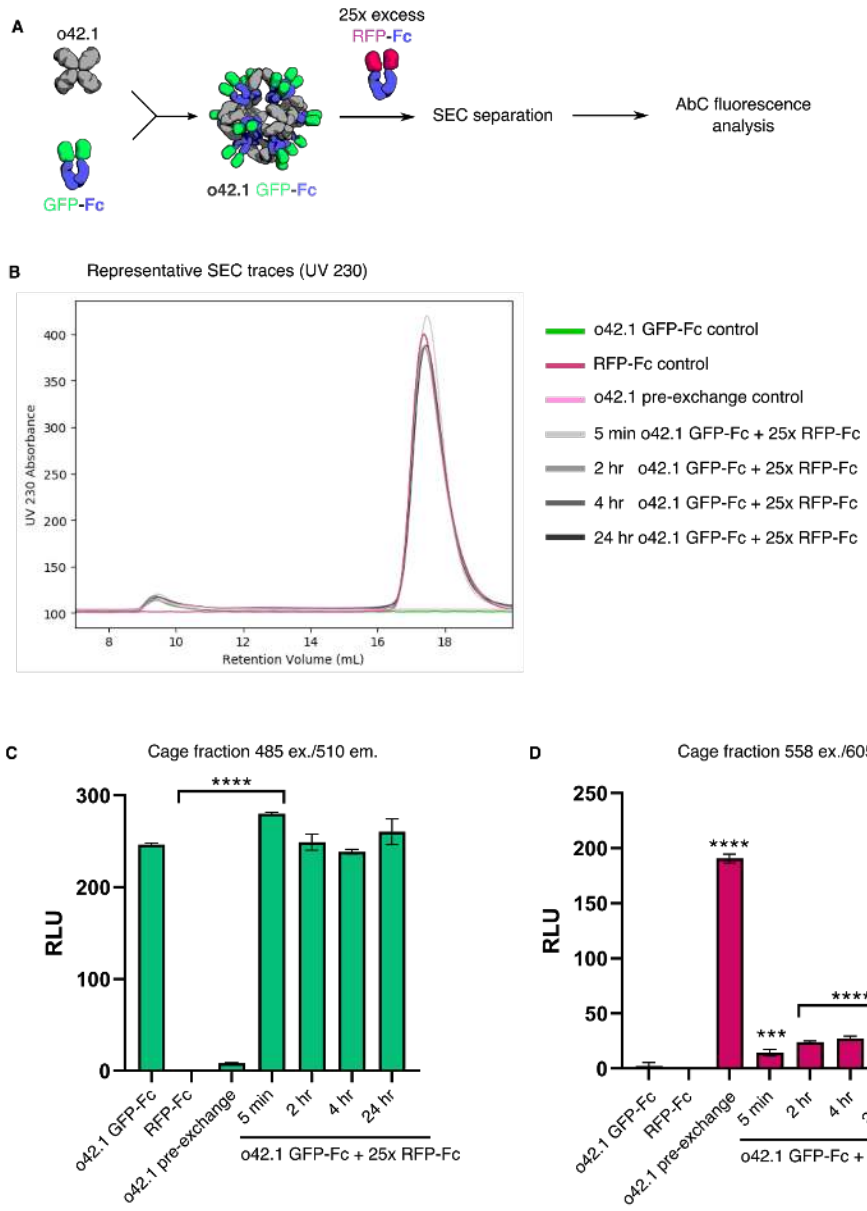

Figure 3.7 Exchange assay using Fc-fluorophore fusions. A, o42.1 AbCs are formed with GFP-Fc, purified, and incubated with 25-fold molar excess of RFP-Fc for up to 24 hours at room temperature. SEC is used to purify cage away from excess Fc-fusion; if AbCs exchange with free Fc-fusions, GFP signal would decrease in the cage fraction as RFP signal increases. Controls include: o42.1 GFP-Fc alone; RFP-Fc alone; and "pre-exchanged" o42.1 AbC prepared by pre-mixing RFP-Fc and GFP-Fc at a 25:1 molar ratio prior to AbC formation. **B,** Representative SEC traces showing UV 230 absorbance. **C,** GFP signal briefly increases in the cage fraction for the o42.1 GFP-Fc AbCs incubated with 25-fold excess RFP-Fc, but drops to control o42.1 GFP-Fc levels, which is maintained for 24 hours at room temperature. **D,** RFP signal is increased in the cage fraction of o42.1 GFP-Fc AbCs incubated with Fc-RFP by less than 20% over 24 hours. See https://zenodo.org/record/4670723 for statistical analyses.

Table 3.1. Antibody cage-forming design success rate. Solubility (column 3) refers to the presence of protein in the post-lysis, post-centrifugation, pre-IMAC soluble fraction as read out by SDS gel. Good SEC component (column 4) refers to SEC traces with some peak corresponding to the approximate predicted size of the nanocage-forming design model. Data for cage formation with Fc are shown in Figs. 3.2 and 3.3.

Geometry	**# ordered**	**Soluble component**	**Good SEC component**	**Forms cage with Fc**
D2 dihedron	6	5	4	3
T32 tetrahedron	11	8	7	2
O32 octahedron	4	3	3	0
O42 octahedron	2	1	1	1
I32 icosahedron	14	14	10	0
I52 icosahedron	11	11	10	2
Total	48	42	35	8

Table 3.2. Details on EM data acquisition.

Sample name	Stain	Magnification	Pixel size (Å /pixiel)	# Micrographs
d2.3 Fc	UF	67,000	1.6	300
d2.4 Fc	UF	67,000	1.6	234
d2.7 Fc	nano-W	67,000	1.6	251
t32.4 Fc	nano-W	67,000	1.6	359
t32.8 Fc	nano-W	67,000	1.6	739
o42.1 Fc	cryo	36,000	1.16	487
i52.3 Fc	cryo	36,000	1.16	460
i52.6 Fc	nano-W	52,000	2.07	342
d2.3 hIgG1	UF	67,000	1.6	331
d2.4 hIgG1	UF	67,000	1.6	160
d2.7 hIgG1	nano-W	67,000	1.6	206
t32.4 hIgG1	nano-W	67,000	1.6	346
t32.8 hIgG1	nano-W	67,000	1.6	193
o42.1 hIgG1	UF	67,000	1.6	525
i52.3 hIgG1	nano-W	52,000	2.07	391
i52.6 hIgG1	nano-W	52,000	2.07	282

Table 3.3. Details on EM data processing.

Sample name	Particle picking	CTF estimation	2D class averages	Ab initio reconstruction and symmetry applied	3D refinement and symmetry applied	# particle in final 3D map/total picked particles	Estimated resolution of 3D map (Å) (*)
d2.3 Fc	cisTEM	cisTEM	cisTEM	cisTEM, D2	cisTEM, D2	8295/11211	-
d2.4 Fc	DoG picker	GCTF	cryoSPARC	cryoSPARC, C1	cryoSPARC, C1	28562/46306	-
d2.7 Fc	cisTEM	cisTEM	cisTEM	cisTEM, D2	cisTEM, D2	17002/24441	-
t32.4 Fc	cisTEM	cisTEM	cisTEM	cisTEM, T2	cisTEM, T2	12416/16806	-
t32.8 Fc	cisTEM	cisTEM	cisTEM	cisTEM, T2	cisTEM, T2	7638/16147	-
o42.1 Fc (cryo-EM)	cryoSPARC Template picking	CTFFIND4 within cryoSPARC	cryoSPARC	cryoSPARC, C1	cryoSPARC, O	4032/16611	11.14
i52.3 Fc (cryo-EM)	cryoSPARC Template picking	CTFFIND4 within cryoSPARC	cryoSPARC	cryoSPARC, C1	cryoSPARC, I	3918/11076	12.18
i52.6 Fc	cisTEM	cisTEM	cisTEM	cisTEM, I2	cisTEM, I2	11801/26436	-
d2.3 hIgG1	cisTEM	cisTEM	cisTEM	-	-	-	-
d2.4 hIgG1	cisTEM	cisTEM	cisTEM	-	-	-	-
d2.7 hIgG1	cisTEM	cisTEM	cisTEM	-	-	-	-
t32.4 hIgG1	cisTEM	cisTEM	cisTEM	-	-	-	-
t32.8 hIgG1	cisTEM	cisTEM	cisTEM	-	-	-	-
o42.1 hIgG1	DoG picker	GCTF	cryoSPARC	-	-	-	-
i52.3 hIgG1	cisTEM	cisTEM	cisTEM	-	-	-	-
i52.6 hIgG1	cisTEM	cisTEM	Relion	-	-	-	-

(*) Negative stain reconstructions obtained had resolution of ~20 Å.

Table 3.4. SAXS data summary. AbC design model predicted data (model) is compared against experimentally-derived SAXS data (exp) for radius of gyration (R_g) and d_{max}. The q_{max} used for analysis is reported. All data were analyzed using ScÅtter3.

Design	R_g model (Å)	R_g exp (Å)	D_{max} model (Å)	D_{max} exp (Å)	q_{max} 1/nm
d2.3	60.69	71.8	210	217	0.21
d2.4	60.67	63.88	210	214	0.25
d2.7	58.95	59.2	197	199	0.25
t32.4	107.27	112.02	280	282	0.25
t32.8	94.39	108.22	263	278	0.17
o42.1	126.48	135.1	320	331	0.16
i52.3	167.73	175.76	427	409	0.15
i52.6	187.32	188.9	454	443	0.15

Chapter 4. Applications of Functionalized Nanocages

The designed AbCs provide a general platform for investigating the effect of valency and geometry on receptor engagement and signaling pathway activation. Receptor dimerization, trimerization and higher order association have been implicated in transmembrane signaling in different receptor systems, but systematically probing the influence on geometry and valency on signaling has required considerable system-specific engineering (*41*). The combination of the wide variety of receptor binding antibodies and natural ligands, with the AbC methodology developed here, in principle allows ready and systematic probing of the effect of geometry and valency of receptor subunit association on signaling for almost any pathway.

To explore the potential of this approach, we assembled antibodies and Fc-fusions targeting a variety of signaling pathways into nanocages and investigated their effects on signaling. Where possible, we attempted to use as many different cage geometries in each application. Typically, only one D2 dihedral design was used as their overall shapes were similar, and design i52.6 was avoided due to stability issues described above.

4.1 Death Receptor 5-mediated Apoptosis

Death Receptor 5 (DR5) is a tumor necrosis factor receptor (TNFR) superfamily cell surface protein that initiates a caspase-mediated apoptotic signaling cascade terminating in cell death when cross-linked by its trimeric native ligand, TNF-related

apoptosis-inducing ligand (TRAIL) (*6*, *42*–*46*). Like other members of the family, DR5 can also form alternative signaling complexes that activate non-apoptotic signaling pathways such as the NF-κB pro-inflammatory pathway and pathways promoting proliferation and migration upon ligand binding (*45*). Because DR5 is overexpressed in some tumors, multiple therapeutic candidates have been developed to activate DR5, such as α-DR5 IgG and recombinant TRAIL, but these have failed clinical trials due to low efficacy and the development of TRAIL resistance in tumor cell populations (*45*, *46*). Combining trimeric TRAIL with bivalent α-DR5 IgG leads to a much stronger apoptotic response than either component by itself, likely due to induction of larger-scale DR5 clustering via the formation of two-dimensional arrays on the cell surface (*43*).

AbCs formed with the same α-DR5 IgG (conatumumab) could have a similar anti-tumor effect without the formation of unbounded arrays; this IgG is particularly interesting as it binds to a separate epitope on DR5 than TRAIL, and thus might be able to overcome TRAIL resistance found in some tumors. Five designs across four geometries were chosen (d2.4, t32.4, t32.8, o42.1, and i52.3) to represent the range of valencies and shapes (Fig. 4.1a). All α-DR5 AbCs were found to form single peaks on SEC with corresponding NS-EM micrographs that were consistent with the formation of assembled particles (Fig. 3.2d-e). All α-DR5 AbCs caused caspase 3/7-mediated apoptosis at similar levels to TRAIL in a colorectal tumor cell line (Colo205), whereas the antibody alone or AbCs formed with bare Fc did not lead to caspase-3/7 activity or cell death, even at the highest concentrations tested (comparing molarity at an antibody to antibody level; Fig. 4.1b). On the TRAIL-resistant renal cell carcinoma line RCC4, all

α-DR5 AbCs induced caspase-3,7 and caspase-8 activity (Fig. 4.1c-e) and designs t32.4, t32.8, and o42.1 greatly reduced cell viability at 150 nM concentration (Fig. 4.1f). Free α-DR5 antibody, Fc-only AbCs, or TRAIL neither activated caspase nor decreased cell viability after four days (Fig. 4.1c-g). Because designs t32.4 and o42.1 activated caspase-3,7 at 100-fold lower concentrations (1.5 nM, Fig. 4.1c), prolonged 6 day treatment of these at 150 nM was tested with RCC4 cells, which resulted in the killing of nearly all cells after six days, suggesting that RCC4 cells do not acquire resistance to the nanocages (Fig. 4.1h). Consistent with the caspase and cell viability data, α-DR5 AbCs increased cleaved PARP (a measure of apoptotic activity) in RCC4 cells, while free α-DR5 antibody, TRAIL or o42.1 Fc AbCs did not result in an increase in cleaved PARP over baseline (Fig. 4.1i-j shows o42.1 as a representative example). The α-DR5 AbCs did not significantly induce apoptosis in healthy primary kidney tubular cells (Fig. 4.1k) (*47*). Please see https://zenodo.org/record/4670723 for statistical analyses, and please see the following reference for methods related to these experiments, as provided by Shally Saini and Julie Mathieu (*1*).

4.2 A1F-Fc AbCs enhance cell proliferation

Certain receptor tyrosine kinases (RTKs), such as the Angiopoietin-1 receptor (Tie2), activate downstream signaling cascades when clustered (*22*, *48*). Scaffolding the F-domain from angiopoietin-1 (A1F) onto nanocages induces phosphorylation of AKT and ERK1/2, enhances cell migration and tube formation *in vitro*, and improves wound healing after injury *in vivo (22)*. Therapeutics with these activities could be useful in

treating conditions characterized by cell death and inflammation, such as sepsis and acute respiratory distress syndrome.

To determine whether the AbC platform could be used to generate such agonists, o42.1 and i52.3 AbCs were assembled with Fc fusions to A1F (Fig. 4.2a-c). The octahedral and icosahedral A1F-AbCs, but not Fc-only controls or free Fc-Ang1F, significantly increased AKT and ERK1/2 phosphorylation above baseline (Fig. 4.2d-e) and enhanced vascular stability (Fig. 4.2f), comparable to an A1F-presenting octamer (*22*). To further address particle stability upon AbC formation, o42.1 A1F-Fc AbCs were incubated for 24 hours with 100% human serum at 4 °C or 37 °C. If AbCs rapidly fell apart or exchanged with serum antibodies, we would likely see a decrease in signal; nonetheless, o42.1 A1F-Fc AbCs in serum retained signaling activity (Fig. 4.2g; quantification was complicated by serum signaling background). Please see https://zenodo.org/record/4670723 for statistical analyses and the following reference for methods related to these experiments, as provided by Yan Ting Zhao, Infencia Xavier, and George Ueda (*1*), adapting published techniques for the tube formation assay (*49*).

4.3 Immune Cell Signaling, CD40, and CD3/CD28

CD40, a TNFR superfamily member expressed on antigen presenting dendritic cells and B cells, is cross-linked by trimeric CD40 ligand (CD40L or CD154) on T cells, leading to signaling and cell proliferation (*50*, *51*). Non-agonistic α-CD40 antibodies can be converted to agonists by adding cross-linkers such as FcγRIIb-expressing Chinese

Hamster Ovary (CHO) cells (*50*). To test if the AbC platform could substitute for the need for cell surface presentation, an α-CD40 IgG (LOB7/6) was assembled into o42.1 AbCs (Fig. 4.3a); this design was selected given its promising data in the DR5 and A1F experiments. SEC and DLS characterization showed the o42.1 α-CD40 LOB7/6 AbCs to be monodisperse and of the expected size (Fig. 4.3b-c). The o42.1 α-CD40 LOB7/6 AbCs were found to induce robust CD40 activation in CD40-expressing reporter CHO cells (J215A, Promega), at concentrations around 20-fold less than a control activating α-CD40 antibody (Promega), while no activation was observed for the free LOB7/6 antibody or octahedral AbC formed with non-CD40 binding IgG (Fig. 4.3d). Nanocage assembly thus converts the non-agonist α-CD40 IgG into a CD40 pathway agonist. Please see https://zenodo.org/record/4670723 for statistical analyses and the following reference for methods related to these experiments, as provided by Marti Tooley (*1*).

T cell engineering technologies such as chimeric antigen receptor (CAR)-T cell therapy require the *ex vivo* expansion and activation of T cells, often carried out by presenting CD3- and CD28-binding ligands on the surface of beads or a plate (*52*, *53*). AbCs formed with both α-CD3 and α-CD28 antibodies could induce activation without the need for the solid support. Equimolar amounts of α-CD3 and α-CD28 were pre-mixed and then incubated with the o42.1 design to form “mosaic” octahedral cages (Fig. 4.4a-c). Octahedral α-CD3/CD28 AbC, but not free antibody or Fc nanocage, led to proliferation of naïve T cells sorted from healthy donor peripheral blood mononuclear cells (PBMCs) as read out by expression of the T cell activation marker CD25 (Fig. 4.4d) and proliferation assays (Fig. 4.4e); activation levels were similar to tetrameric or

plate-bound α-CD3/CD28 stimulation controls. Together with the α-CD40 activation, these results demonstrate how readily specific immune cell pathways can be activated by simply swapping in different antibodies into the cage architecture. Please see the following reference for methods related to these experiments, as provided by Peter Morawski, Mitch Fahning, and Daniel Campbell (*1*).

4.3 SARS-CoV-2 Spike Targeted Neutralization

Antibodies targeting the SARS-CoV-2 spike (S) protein are crucial for treatments related to prophylaxis and post-exposure therapy for the COVID-19 pandemic (*54–60*). By assembling α-SARS-CoV-2 antibodies into nanocages, the antibodies' neutralization potencies could be increased by increasing avidity for viral particles, as multivalency was recently found to increase SARS-CoV-2 neutralization using apoferritin to scaffold binding domains (*56*). Octahedral AbCs (o42.1) formed with the SARS-CoV-2 S-binding antibodies CV1 or CV30 (*54*) were more effective at neutralizing pseudovirus entry into angiotensin-converting enzyme 2 (ACE2)-expressing cells than free CV1 or CV30, dropping the apparent IC_{50} over 200-fold and around 2.5-fold, respectively (comparing molarity at an antibody to antibody level; Fig. 4.5a-c). The potency of a third non-neutralizing antibody, CV3, was unchanged by assembly into the nanocage format (Fig. 4.5d). We found that assembling Fc-ACE2, which directly engages the receptor binding domain of the spike protein (*60*), with the octahedral AbC-forming design enhanced neutralization around 7-fold compared to free Fc-ACE2 fusion for SARS-CoV-2 pseudovirus and 2.5-fold for SARS-CoV-1 pseudovirus (Fig. 4.5e-f).

Please see https://zenodo.org/record/4670723 for statistical analyses and the following reference for methods related to these experiments, as provided by the labs of Andy McGuire and Leo Stamatatos (IgG neutralization) or Ha Dang, Lexi Walls, and David Veesler (Fc-ACE2) (*1*), adapting published techniques for preparing the pseudovirus and and ACE2-expressing cells (*60*, *61*).

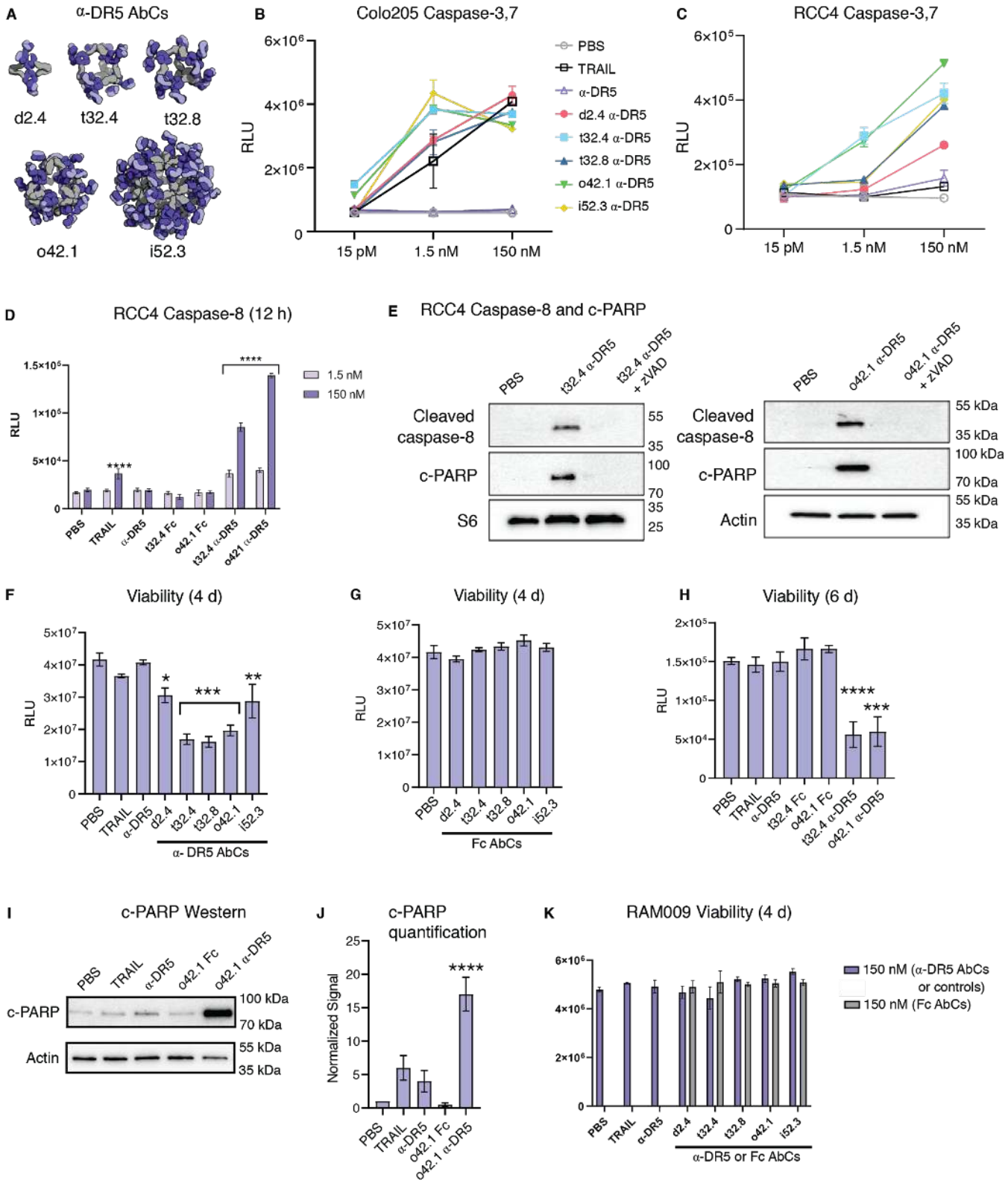
A
α-DR5 AbCs
d2.4
t32.4
t32.8
o42.1
i52.3
B
Colo205 Caspase-3,7
RLU
PBS
TRAIL
α-DR5
d2.4 α-DR5
t32.4 α-DR5
t32.8 α-DR5
o42.1 α-DR5
i52.3 α-DR5
15 pM
1.5 nM
150 nM
C
RCC4 Caspase-3,7
D
RCC4 Caspase-8 (12 h)
1.5 nM
150 nM
E
RCC4 Caspase-8 and c-PARP
Cleaved caspase-8
c-PARP
S6
Actin
+ zVAD
F
Viability (4 d)
α- DR5 AbCs
G
Viability (4 d)
Fc AbCs
H
Viability (6 d)
I
c-PARP Western
J
c-PARP quantification
Normalized Signal
K
RAM009 Viability (4 d)
150 nM (α-DR5 AbCs or controls)
150 nM (Fc AbCs)
α-DR5 or Fc AbCs

Figure 4.1. AbCs targeting DR5 kill TRAIL-resistant cells. A-B, Caspase-3,7 is activated by AbCs formed with α-DR5 antibody (**A**), but not the free antibody, in Colo205 colorectal cells (**B**) and RCC4 renal cancer cells (**C**). **D,** α-DR5 t32.4 and o42.1 AbCs activate caspase-8 after 12 hour incubation in RCC4 cells. **E**, Cleaved-caspase 8 and cleaved-PARP inhibition after 24 hour incubation with t32.4 and o42.1 α-DR5 AbCs, and 10 μM zVAD, a caspase inhibitor. **F-G**, α-DR5 AbCs (**F**), but not Fc AbC controls (**G**) reduce RCC4 cell viability 4 days after treatment. **H**, α-DR5 AbCs reduce RCC4 viability 6 days after treatment. **I-J**, o42.1 α-DR5 AbCs enhance PARP cleavage, a marker of apoptotic signaling; **J**, quantification of **I** relative to PBS control. **K,** α-DR5 AbCs do not reduce viability in a primary tubular kidney cell line (RAM009). Statistical analyses are reported in https://zenodo.org/record/4670723.

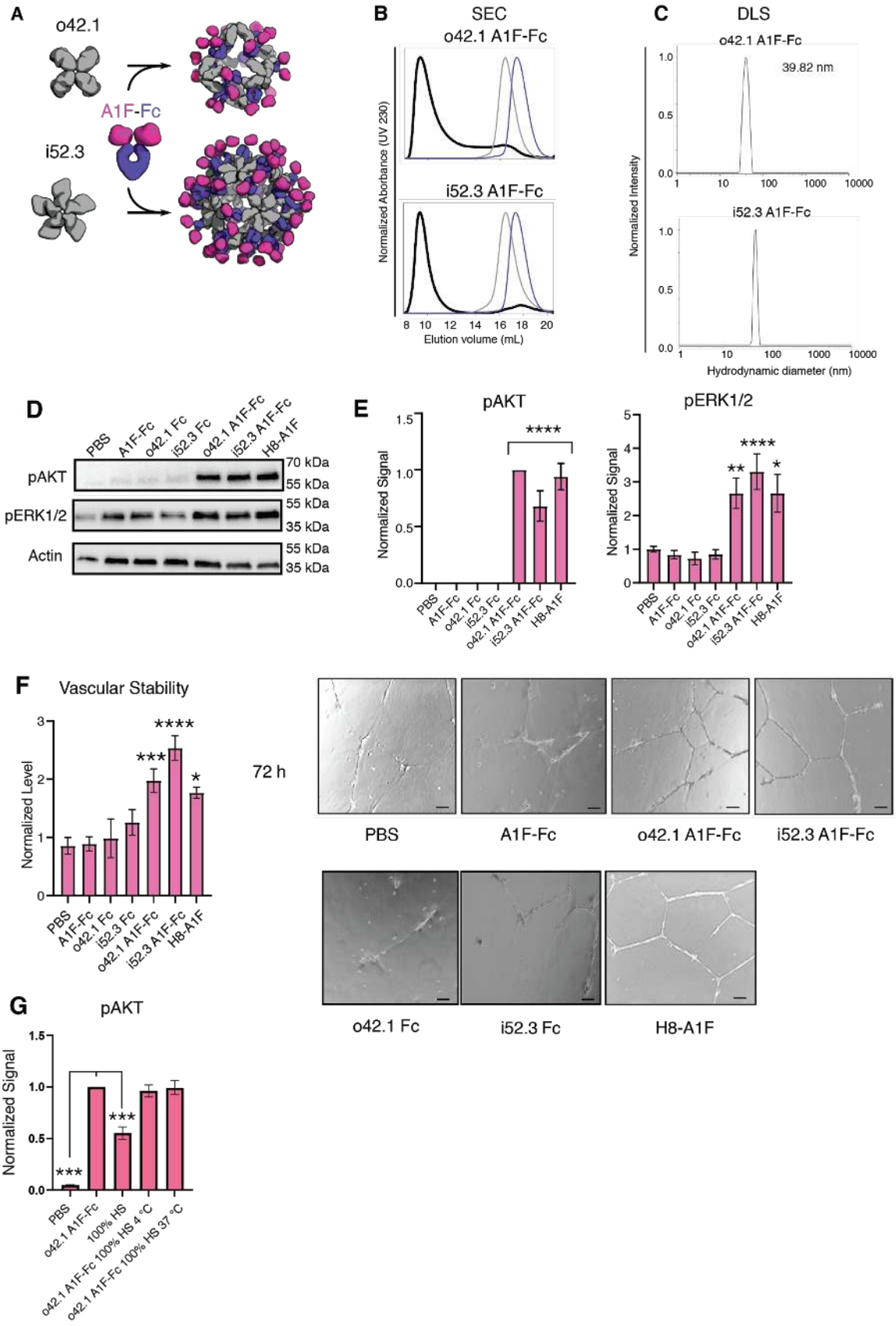
A
o42.1
A1F-Fc
i52.3
B
SEC
o42.1 A1F-Fc
i52.3 A1F-Fc
Normalized Aborbance (UV 230)
8 10 12 14 16 18 20
Elution volume (mL)
C
DLS
o42.1 A1F-Fc
39.82 nm
i52.3 A1F-Fc
Normalized Intensity
Hydrodynamic diameter (nm)
D
PBS
A1F-Fc
o42.1 Fc
i52.3 Fc
o42.1 A1F-Fc
i52.3 A1F-Fc
H8-A1F
pAKT
pERK1/2
Actin
70 kDa
55 kDa
55 kDa
35 kDa
55 kDa
35 kDa
E
pAKT
pERK1/2
Normalized Signal
****
**
*
F
Vascular Stability
Normalized Level
72 h
PBS
A1F-Fc
o42.1 A1F-Fc
i52.3 A1F-Fc
o42.1 Fc
i52.3 Fc
H8-A1F
G
pAKT
Normalized Signal
PBS
o42.1 A1F-Fc
100% HS
o42.1 A1F-Fc 100% HS 4 °C
o42.1 A1F-Fc 100% HS 37 °C

Figure 4.2. A1F-Fc AbCs enhance cell proliferation. A-C, o42.1 and i52.3 AbCs formed with A1F-Fc (**A**) are monodisperse and of the expected size per SEC on a Superose 6 column (**B**) and DLS (**C**). SEC shows the assembly trace in black, the relevant AbC design component in grey, and the A1F-Fc in purple. **D**, Representative Western blots show that A1F-Fc AbCs, but not negative controls, increase pAKT and pERK1/2 signals. **E**, quantification of **D**: pAKT quantification is normalized to o42.1 A1F-Fc signaling (due to no pAKT signal in the PBS control); pERK1/2 is normalized to PBS. **F**, A1F-Fc AbCs increase vascular stability after 72 hours. Left: quantification of vascular stability compared to PBS. Right: representative images; scale bars are 100 μm. **G,** o42.1 A1F-Fc AbCs were incubated with 100% human serum (HS) for 24 hours at 4 °C or 37 °C and applied to HUVEC cells at 150 nM. pAKT signal showed no decrease from o42.1 A1F-Fc particles incubated with serum. All error bars represent means ± SEM; means were compared using ANOVA and Dunnett post-hoc tests (https://zenodo.org/record/4670723).

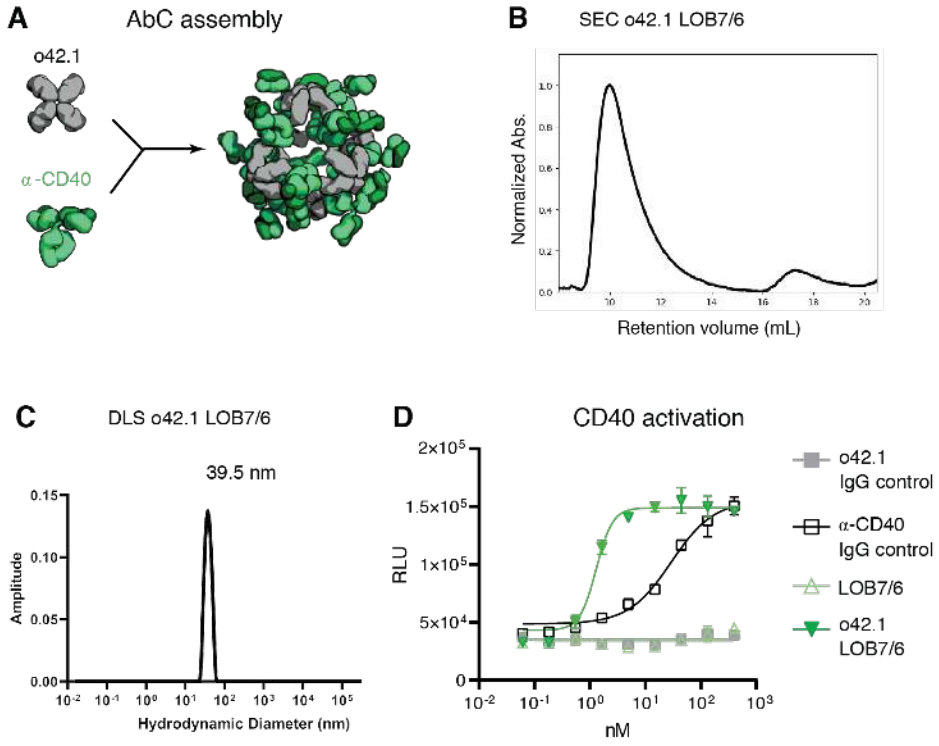

Figure 4.3. AbCs convert an α-CD40 antagonist antibody into an agonist. A-C, α-CD40 AbCs (clone LOB7/6, **A**) formed with o42.1, were structurally verified using an SEC Superose 6 column (**B**) and DLS (**C**). **D,** CD40 pathways are activated by α-CD40 LOB7/6 octahedral nanocages but not by free α-CD40 LOB7/6 or controls. Error bars represent means ± SD, n=3; EC50s reported in https://zenodo.org/record/4670723**.**

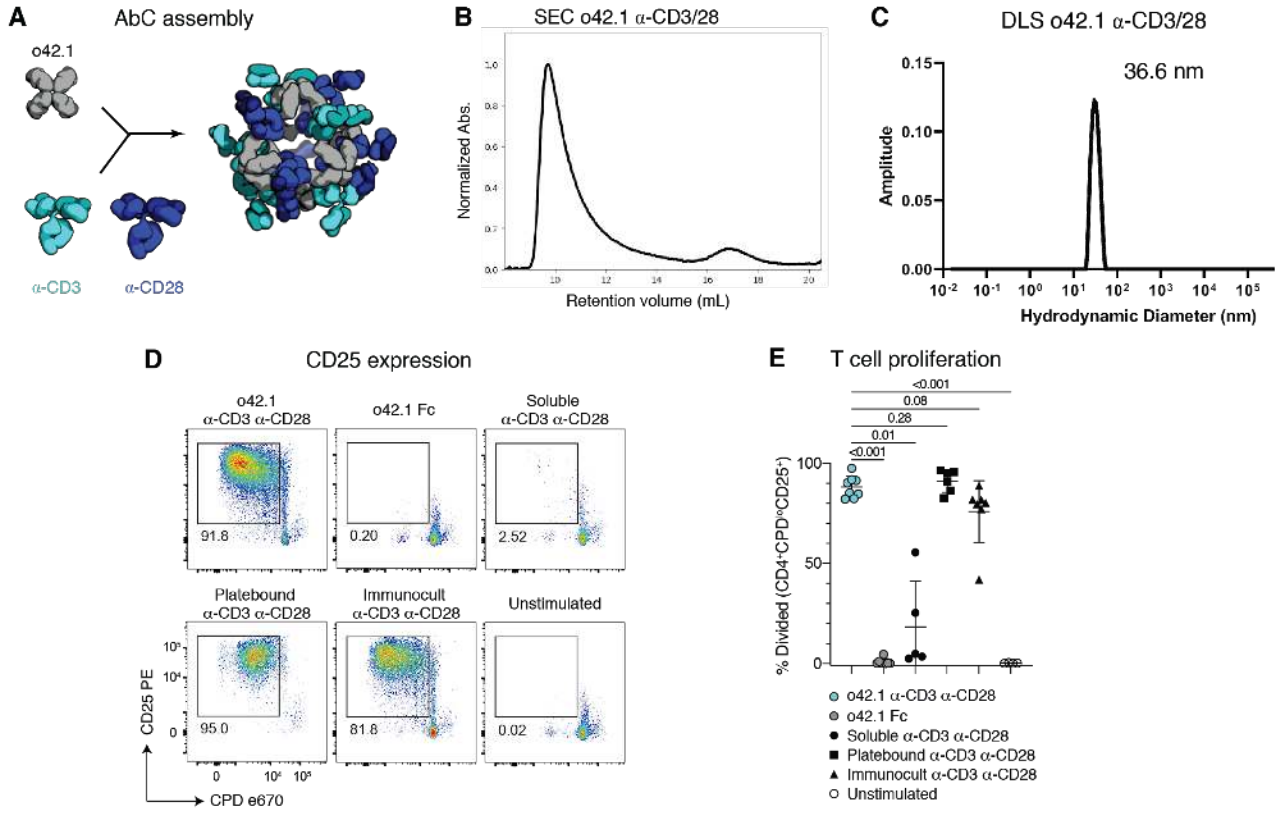

Figure 4.4. α-CD3/28 mosaic AbCs cause T-cell proliferation. A-C, α-CD3 and α-CD28 mosaic AbCs were assembled with o42.1, and were structurally verified using an SEC Superose 6 column (**B**) and DLS (**C**). **D,** Representative plots show the frequency of dividing, activated cells ($CPD^{lo}CD25^{+}$). Mosaic AbC-induced proliferation is comparable to traditional positive controls, platebound or tetrameric α-CD3 α-CD28 antibody bead complex (Immunocult). Gated on live $CD4^{+}$ T cells. **E,** Summary graph shows mean ± SD. Significance was determined by Kruskal-Wallis tests correcting for multiple comparisons using FDR two-stage method (n=4-8 per condition). Adjusted p values are reported. CPD, Cell Proliferation Dye.

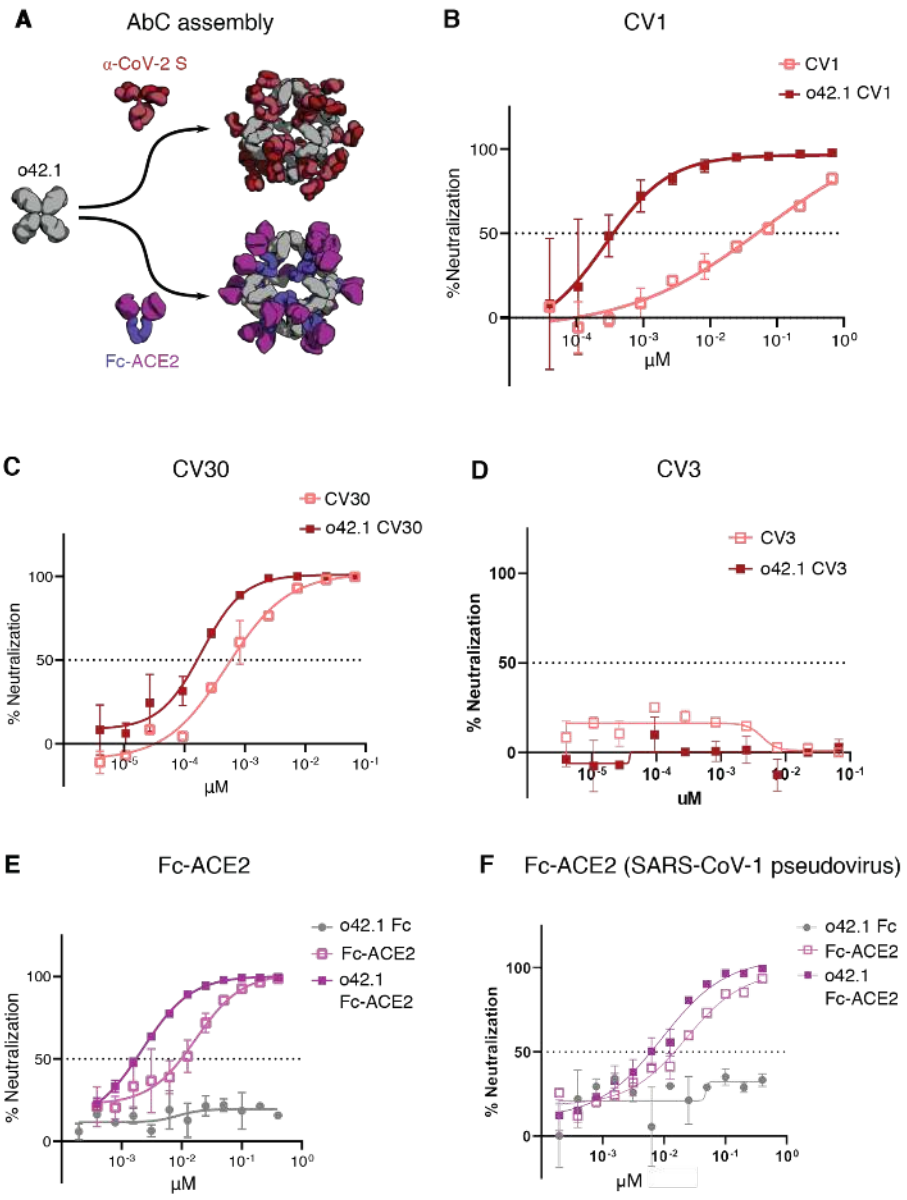

Figure 4.5 S-targeting AbCs enhance neutralization of CoV pseudoviruses. A, Octahedral AbCs are produced with either α-CoV-2 S IgGs or Fc-ACE2 fusion. **B-D,** SARS-CoV-2 S pseudovirus neutralization by octahedral AbC formed with α-CoV-2 S IgGs CV1 (**B**), CV30 (**C**), CV3 (**D**) compared to un-caged IgG. **E-F,** SARS-CoV-2 (**E**) or SARS-CoV-1 (**F**) pseudovirus neutralization by Fc-ACE2 octahedral AbC compared to un-caged Fc-ACE2. Error bars represent means ± SD, n=2; IC50s reported in https://zenodo.org/record/4670723.

Chapter 5. Discussion and Future Directions

Designed AbCs go beyond previous computational design efforts to create functional nanomaterials by integrating form and function; whereas previous work has fused functional domains onto assemblies constructed from separate structural components (*3*–*15*, *42*), AbCs employ antibodies as both structural and functional components. By fashioning designed antibody-binding, cage-forming oligomers through rigid helical fusion, a wide range of geometries and orientations was achieved.

This design strategy can be generalized to incorporate other homo-oligomers of interest into cage-like architectures. For example, nanocages could be assembled with viral glycoprotein antigens using components terminating in helical antigen-binding proteins, or from symmetric enzymes with exposed helices available for fusion to maximize the proximity of active sites working on successive reactions. The AbCs offer considerable advantages in modularity compared to previous fusion of functional domain approaches; any of the thousands of known antibodies can be used "off-the-shelf" to form multivalent cages by mixing with the appropriate design to form the desired symmetric assembly, provided sufficient protein A/Fc affinity in the IgG allotype (Tables 5.1, 5.2). EM and SEC demonstrate monodispersity comparable to IgM and control over binding domain valency and positioning that is not (to our knowledge) attained by other antibody-protein nanoparticle formulations (*62*).

AbCs show considerable promise as signaling pathway agonists. Assembly of antibodies against RTK- and TNFR-family cell-surface receptors into AbCs led to

activation of diverse downstream signaling pathways involved in cell death, proliferation, and differentiation. While antibody-mediated clustering has been previously found to activate signaling pathways (*43*, *50*), this approach has the advantage of much higher structural homogeneity, allowing more precise tuning of phenotypic effects and more controlled formulation. Two or more different receptor engaging antibodies or Fc-fusions can be readily incorporated into the same cage by simple mixing, allowing exploration of the effects on downstream signaling by bringing together different receptors and comodulators in different valencies and geometries. There are exciting applications to targeted delivery, as the icosahedral AbCs have substantial internal volume (around 15,000 nm^3, based on an estimated interior radius of 15.5 nm) that could be used to package nucleic acid or protein cargo, and achieving different target specificity in principle is as simple as swapping one antibody for another.

An important next step towards the possibility of augmenting antibody therapeutics with the designed AbCs-forming oligomers will be investigating the pharmacokinetic and biodistribution properties of these molecules, their immunogenicity, and whether the Fc domains can still activate effector functions. For effector functions, in theory the AbC architecture should not block Fc gamma receptors or C1q from binding to previously-determined N-terminal residues in the Fc CH2 domains, but the full C1 complex would appear to be unable to form without AbC disassembly (*63*). I hope that the AbCs developed here, coupled with the very large repertoire of existing antibodies bound by protein A, will be broadly useful across a wide range of applications.

Table 5.1. List of antibodies formed into cages. Successfully formed cages (by SEC) listed by the antibody target reactivity, antibody species and isotype, and designs used.

Ab reactivity	Ab subclass	Designs (validated by SEC at minimum)	Comments
α-CD3	mIgG2a	t32.4, o42.1	OKT3
α-CD4	mIgG2b	o42.1	OKT4
α-CD28	hIgG1	t32.4, o42.1	CD28.6
α-CD40	mIgG2a or mIgG2b	o42.1	LOB7/6 or 82111 (respectively)
α-CoV2 S	hIgG1	o42.1	CV1, CV3, CV30
α-DR5 (human)	hIgG1	d2.3, d2.4, d2.7, t32.4, t32.8, o42.1, i52.3, i52.6	conatumumab
α-DR5 (mouse)	Armenian hamster IgG	t32.4, o42.1	MD5-1
α-EGFR	hIgG1	mIgG2b	cetuximab
α-LRP6	hIgG1	t32.4, o42.1	YW210.09
α-RSV F	hIgG1	d2.3, d2.4, d2.7, t32.4, t32.8, o42.1, i52.3, i52.6	mpe8
Non-specific	Rabbit IgG	d2.4, o42.1	Rabbit serum IgG

Table 5.2. List of Fc-fusions formed into cages.. Successfully formed cages (by SEC) listed by the ligand that was fused to Fc, the Fc sequence species and isotype, and designs used

Fc-fusion ligand	Fc subclass	Designs (validated by SEC at minimum)	Comments
Angiopoietin-1 F-domain	hIgG1	d2.4, t32.4, t32.8, o42.1, i52.3	
Angiotensin-converting enzyme 2 (ACE2)	hIgG1	o42.1	
CD80	hIgG1	o42.1	
mRuby2	hIgG1	d2.4, t32.4, t32.8, o42.1, i52.3	
sfGFP	hIgG1	d2.4, t32.4, t32.8, o42.1, i52.3	
VEGF-a	hIgG1	t32.4, o42.1	
VEGF-c	hIgG1	t32.4, o42.1	

Bibliography

1. R. Divine, H. V. Dang, G. Ueda, J. A. Fallas, I. Vulovic, W. Sheffler, S. Saini, Y. T. Zhao, I. X. Raj, P. A. Morawski, M. F. Jennewein, L. J. Homad, Y.-H. Wan, M. R. Tooley, F. Seeger, A. Etemadi, M. L. Fahning, J. Lazarovits, A. Roederer, A. C. Walls, L. Stewart, M. Mazloomi, N. P. King, D. J. Campbell, A. T. McGuire, L. Stamatatos, H. Ruohola-Baker, J. Mathieu, D. Veesler, D. Baker, Designed proteins assemble antibodies into modular nanocages. *Science*. **372** (2021), doi:10.1126/science.abd9994.

2. R.-M. Lu, Y.-C. Hwang, I.-J. Liu, C.-C. Lee, H.-Z. Tsai, H.-J. Li, H.-C. Wu, Development of therapeutic antibodies for the treatment of diseases. *J. Biomed. Sci.* **27**, 1–30 (2020).

3. A. M. Cuesta, N. Sainz-Pastor, J. Bonet, B. Oliva, L. Alvarez-Vallina, Multivalent antibodies: when design surpasses evolution. *Trends Biotechnol.* **28**, 355–362 (2010).

4. N. Nuñez-Prado, M. Compte, S. Harwood, A. Álvarez-Méndez, S. Lykkemark, L. Sanz, L. Álvarez-Vallina, The coming of age of engineered multivalent antibodies. *Drug Discov. Today*. **20**, 588–594 (2015).

5. N. S. Laursen, R. H. E. Friesen, X. Zhu, M. Jongeneelen, S. Blokland, J. Vermond, A. van Eijgen, C. Tang, H. van Diepen, G. Obmolova, M. van der Neut Kolfschoten, D. Zuijdgeest, R. Straetemans, R. M. B. Hoffman, T. Nieusma, J. Pallesen, H. L. Turner, S. M. Bernard, A. B. Ward, J. Luo, L. L. M. Poon, A. P. Tretiakova, J. M. Wilson, M. P. Limberis, R. Vogels, B. Brandenburg, J. A. Kolkman, I. A. Wilson, Universal protection against influenza infection by a multidomain antibody to influenza hemagglutinin. *Science*. **362**, 598–602 (2018).

6. O. Seifert, A. Plappert, S. Fellermeier, M. Siegemund, K. Pfizenmaier, R. E. Kontermann, Tetravalent antibody-scTRAIL fusion proteins with improved properties. *Mol. Cancer Ther.* **13**, 101–111 (2014).

7. T. F. Rowley, S. J. Peters, M. Aylott, R. Griffin, N. L. Davies, L. J. Healy, R. M. Cutler, A. Eddleston, T. L. Pither, J. M. Sopp, O. Zaccheo, G. Fossati, K. Cain, A. M. Ventom, H. Hailu, E. J. Ward, J. Sherington, F. R. Brennan, F. Fallah-Arani, D. P. Humphreys, Engineered hexavalent Fc proteins with enhanced Fc-gamma receptor avidity provide insights into immune-complex interactions. *Commun Biol*. **1**, 146 (2018).

8. Various methods of gold nanoparticles (GNPs) conjugation to antibodies. *Sensing and Bio-Sensing Research*. **9**, 17–22 (2016).

9. R. S. Riley, E. S. Day, Frizzled7 Antibody-Functionalized Nanoshells Enable Multivalent Binding for Wnt Signaling Inhibition in Triple Negative Breast Cancer Cells. *Small*. **13** (2017), doi:10.1002/smll.201700544.

10. A. Miller, S. Carr, T. Rabbitts, H. Ali, Multimeric antibodies with increased valency surpassing functional affinity and potency thresholds using novel formats. *MAbs*. **12**, 1752529 (2020).

11. H. J. Kang, Y. J. Kang, Y.-M. Lee, H.-H. Shin, S. J. Chung, S. Kang, Developing an

antibody-binding protein cage as a molecular recognition drug modular nanoplatform. *Biomaterials*. **33**, 5423–5430 (2012).

12. H. Kim, Y. J. Kang, J. Min, H. Choi, S. Kang, Development of an antibody-binding modular nanoplatform for antibody-guided targeted cell imaging and delivery. *RSC Advances*. **6** (2016), pp. 19208–19213.

13. S. I. Lim, C. I. Lukianov, J. A. Champion, Self-assembled protein nanocarrier for intracellular delivery of antibody. *J. Control. Release*. **249**, 1–10 (2017).

14. K. Uhde-Holzem, M. McBurney, B. D. B. Tiu, R. C. Advincula, R. Fischer, U. Commandeur, N. F. Steinmetz, Production of Immunoabsorbent Nanoparticles by Displaying Single-Domain Protein A on Potato Virus X. *Macromol. Biosci.* **16**, 231–241 (2016).

15. C. Lee, S. Peddi, C. Anderson, H. Su, H. Cui, A. L. Epstein, J. A. MacKay, Adaptable antibody Nanoworms designed for non-Hodgkin lymphoma. *Biomaterials*. **262**, 120338 (2020).

16. T. O. Yeates, Y. Liu, J. Laniado, The design of symmetric protein nanomaterials comes of age in theory and practice. *Curr. Opin. Struct. Biol.* **39**, 134–143 (2016).

17. G. Ueda, A. Antanasijevic, J. A. Fallas, W. Sheffler, J. Copps, D. Ellis, G. Hutchinson, A. Moyer, A. Yasmeen, Y. Tsybovsky, Y.-J. Park, M. J. Bick, B. Sankaran, R. A. Gillespie, P. J. M. Brouwer, P. H. Zwart, D. Veesler, M. Kanekiyo, B. S. Graham, R. Sanders, J. P. Moore, P. J. Klasse, A. B. Ward, N. King, D. Baker, Tailored Design of Protein Nanoparticle Scaffolds for Multivalent Presentation of Viral Glycoprotein Antigens. *eLife* **9**, e57659 (2020).

18. J. B. Bale, S. Gonen, Y. Liu, W. Sheffler, D. Ellis, C. Thomas, D. Cascio, T. O. Yeates, T. Gonen, N. P. King, D. Baker, Accurate design of megadalton-scale two-component icosahedral protein complexes. *Science*. **353**, 389–394 (2016).

19. I. Vulovic, Q. Yao, Y.-J. Park, A. Courbet, A. Norris, F. Busch, A. Sahasrabuddhe, H. Merten, D. D. Sahtoe, G. Ueda, J. A. Fallas, S. J. Weaver, Y. Hsia, R. A. Langan, A. Plückthun, V. H. Wysocki, D. Veesler, G. J. Jensen, D. Baker, Generation of ordered protein assemblies using rigid three-body fusion. *bioRxiv* (2020), p. 2020.07.18.210294.

20. Y. Hsia, R. Mout, W. Sheffler, N. I. Edman, I. Vulovic, Y.-J. Park, R. L. Redler, M. J. Bick, A. K. Bera, A. Courbet, A. Kang, T. J. Brunette, U. Nattermann, E. Tsai, A. Saleem, C. M. Chow, D. Ekiert, G. Bhabha, D. Veesler, D. Baker, Hierarchical design of multi-scale protein complexes by combinatorial assembly of oligomeric helical bundle and repeat protein building blocks (2020).

21. K. A. Cannon, V. N. Nguyen, C. Morgan, T. O. Yeates, Design and Characterization of an Icosahedral Protein Cage Formed by a Double-Fusion Protein Containing Three Distinct Symmetry Elements. *ACS Synth. Biol.* **9**, 517–524 (2020).

22. Y. T. Zhao, J. A. Fallas, S. Saini, G. Ueda, L. Somasundaram, Z. Zhou, I. Xavier, D. Ehnes, C. Xu, L. Carter, S. Wrenn, J. Mathieu, D. L. Sellers, D. Baker, H. Ruohola-Baker, F-domain valency determines outcome of signaling through the angiopoietin pathway. *bioRxiv* (2020),

p. 2020.09.19.304188.

23. M. Graille, E. A. Stura, A. L. Corper, B. J. Sutton, M. J. Taussig, J. B. Charbonnier, G. J. Silverman, Crystal structure of a Staphylococcus aureus protein A domain complexed with the Fab fragment of a human IgM antibody: structural basis for recognition of B-cell receptors and superantigen activity. *Proc. Natl. Acad. Sci. U. S. A.* **97**, 5399–5404 (2000).

24. E. E. Idusogie, L. G. Presta, H. Gazzano-Santoro, K. Totpal, P. Y. Wong, M. Ultsch, Y. G. Meng, M. G. Mulkerrin, Mapping of the C1q binding site on rituxan, a chimeric antibody with a human IgG1 Fc. *J. Immunol.* **164**, 4178–4184 (2000).

25. F. DiMaio, N. Echols, J. J. Headd, T. C. Terwilliger, P. D. Adams, D. Baker, Improved low-resolution crystallographic refinement with Phenix and Rosetta. *Nature Methods*. **10** (2013), pp. 1102–1104.

26. E. T. Boder, K. D. Wittrup, Optimal screening of surface-displayed polypeptide libraries. *Biotechnol. Prog.* **14**, 55–62 (1998).

27. T. J. Brunette, F. Parmeggiani, P.-S. Huang, G. Bhabha, D. C. Ekiert, S. E. Tsutakawa, G. L. Hura, J. A. Tainer, D. Baker, Exploring the repeat protein universe through computational protein design. *Nature*. **528**, 580–584 (2015).

28. J. A. Fallas, G. Ueda, W. Sheffler, V. Nguyen, D. E. McNamara, B. Sankaran, J. H. Pereira, F. Parmeggiani, T. J. Brunette, D. Cascio, T. R. Yeates, P. Zwart, D. Baker, Computational design of self-assembling cyclic protein homo-oligomers. *Nat. Chem.* **9**, 353–360 (2017).

29. Y. Hsia, J. B. Bale, S. Gonen, D. Shi, W. Sheffler, K. K. Fong, U. Nattermann, C. Xu, P.-S. Huang, R. Ravichandran, S. Yi, T. N. Davis, T. Gonen, N. P. King, D. Baker, Design of a hyperstable 60-subunit protein dodecahedron. [corrected]. *Nature*. **535**, 136–139 (2016).

30. J. K. Leman, B. D. Weitzner, S. M. Lewis, J. Adolf-Bryfogle, N. Alam, R. F. Alford, M. Aprahamian, D. Baker, K. A. Barlow, P. Barth, B. Basanta, B. J. Bender, K. Blacklock, J. Bonet, S. E. Boyken, P. Bradley, C. Bystroff, P. Conway, S. Cooper, B. E. Correia, B. Coventry, R. Das, R. M. De Jong, F. DiMaio, L. Dsilva, R. Dunbrack, A. S. Ford, B. Frenz, D. Y. Fu, C. Geniesse, L. Goldschmidt, R. Gowthaman, J. J. Gray, D. Gront, S. Guffy, S. Horowitz, P.-S. Huang, T. Huber, T. M. Jacobs, J. R. Jeliazkov, D. K. Johnson, K. Kappel, J. Karanicolas, H. Khakzad, K. R. Khar, S. D. Khare, F. Khatib, A. Khramushin, I. C. King, R. Kleffner, B. Koepnick, T. Kortemme, G. Kuenze, B. Kuhlman, D. Kuroda, J. W. Labonte, J. K. Lai, G. Lapidoth, A. Leaver-Fay, S. Lindert, T. Linsky, N. London, J. H. Lubin, S. Lyskov, J. Maguire, L. Malmström, E. Marcos, O. Marcu, N. A. Marze, J. Meiler, R. Moretti, V. K. Mulligan, S. Nerli, C. Norn, S. Ó'Conchúir, N. Ollikainen, S. Ovchinnikov, M. S. Pacella, X. Pan, H. Park, R. E. Pavlovicz, M. Pethe, B. G. Pierce, K. B. Pilla, B. Raveh, P. Douglas Renfrew, S. S. Roy Burman, A. Rubenstein, M. F. Sauer, A. Scheck, W. Schief, O. Schueler-Furman, Y. Sedan, A. M. Sevy, N. G. Sgourakis, L. Shi, J. B. Siegel, D.-A. Silva, S. Smith, Y. Song, A. Stein, M. Szegedy, F. D. Teets, S. B. Thyme, R. Y.-R. Wang, A. Watkins, L. Zimmerman, R. Bonneau, Macromolecular modeling and design in Rosetta: recent methods and frameworks. *Nat. Methods*. **17**, 665–680 (2020).

31. F. W. Studier, F. William Studier, Protein production by auto-induction in high-density

shaking cultures. *Protein Expression and Purification*. **41** (2005), pp. 207–234.

32. B. M. Baynes, D. I. C. Wang, B. L. Trout, Role of arginine in the stabilization of proteins against aggregation. *Biochemistry*. **44**, 4919–4925 (2005).

33. D. Corti, S. Bianchi, F. Vanzetta, A. Minola, L. Perez, G. Agatic, B. Guarino, C. Silacci, J. Marcandalli, B. J. Marsland, A. Piralla, E. Percivalle, F. Sallusto, F. Baldanti, A. Lanzavecchia, Cross-neutralization of four paramyxoviruses by a human monoclonal antibody. *Nature*. **501**, 439–443 (2013).

34. D. Tegunov, P. Cramer, Real-time cryo-electron microscopy data preprocessing with Warp. *Nat. Methods*. **16**, 1146–1152 (2019).

35. S. H. W. Scheres, S. Chen, Prevention of overfitting in cryo-EM structure determination. *Nat. Methods*. **9**, 853–854 (2012).

36. P. B. Rosenthal, R. Henderson, Optimal determination of particle orientation, absolute hand, and contrast loss in single-particle electron cryomicroscopy. *J. Mol. Biol.* **333**, 721–745 (2003).

37. S. Chen, G. McMullan, A. R. Faruqi, G. N. Murshudov, J. M. Short, S. H. W. Scheres, R. Henderson, High-resolution noise substitution to measure overfitting and validate resolution in 3D structure determination by single particle electron cryomicroscopy. *Ultramicroscopy*. **135**, 24–35 (2013).

38. K. N. Dyer, M. Hammel, R. P. Rambo, S. E. Tsutakawa, I. Rodic, S. Classen, J. A. Tainer, G. L. Hura, High-throughput SAXS for the characterization of biomolecules in solution: a practical approach. *Methods Mol. Biol.* **1091**, 245–258 (2014).

39. D. Schneidman-Duhovny, M. Hammel, J. A. Tainer, A. Sali, Accurate SAXS profile computation and its assessment by contrast variation experiments. *Biophys. J.* **105**, 962–974 (2013).

40. P. B. Moore, Small-angle scattering. Information content and error analysis. *Journal of Applied Crystallography*. **13** (1980), pp. 168–175.

41. K. Mohan, G. Ueda, A. R. Kim, K. M. Jude, J. A. Fallas, Y. Guo, M. Hafer, Y. Miao, R. A. Saxton, J. Piehler, V. G. Sankaran, D. Baker, K. C. Garcia, Topological control of cytokine receptor signaling induces differential effects in hematopoiesis. *Science*. **364** (2019), doi:10.1126/science.aav7532.

42. M. Siegemund, F. Schneider, M. Hutt, O. Seifert, I. Müller, D. Kulms, K. Pfizenmaier, R. E. Kontermann, IgG-single-chain TRAIL fusion proteins for tumour therapy. *Sci. Rep.* **8**, 1–11 (2018).

43. J. D. Graves, J. J. Kordich, T.-H. Huang, J. Piasecki, T. L. Bush, T. Sullivan, I. N. Foltz, W. Chang, H. Douangpanya, T. Dang, J. W. O'Neill, R. Mallari, X. Zhao, D. G. Branstetter, J. M. Rossi, A. M. Long, X. Huang, P. M. Holland, Apo2L/TRAIL and the death receptor 5 agonist antibody AMG 655 cooperate to promote receptor clustering and antitumor activity. *Cancer*

Cell. **26**, 177–189 (2014).

44. J. Naval, D. de Miguel, A. Gallego-Lleyda, A. Anel, L. Martinez-Lostao, Importance of TRAIL Molecular Anatomy in Receptor Oligomerization and Signaling. Implications for Cancer Therapy. *Cancers* . **11** (2019), doi:10.3390/cancers11040444.

45. D. de Miguel, J. Lemke, A. Anel, H. Walczak, L. Martinez-Lostao, Onto better TRAILs for cancer treatment. *Cell Death Differ.* **23**, 733–747 (2016).

46. M. H. Tuthill, A. Montinaro, J. Zinngrebe, K. Prieske, P. Draber, S. Prieske, T. Newsom-Davis, S. von Karstedt, J. Graves, H. Walczak, TRAIL-R2-specific antibodies and recombinant TRAIL can synergise to kill cancer cells. *Oncogene*. **34** (2015), pp. 2138–2144.

47. J. Mathieu, Z. Zhang, W. Zhou, A. J. Wang, J. M. Heddleston, C. M. A. Pinna, A. Hubaud, B. Stadler, M. Choi, M. Bar, M. Tewari, A. Liu, R. Vessella, R. Rostomily, D. Born, M. Horwitz, C. Ware, C. A. Blau, M. A. Cleary, J. N. Rich, H. Ruohola-Baker, HIF induces human embryonic stem cell markers in cancer cells. *Cancer Res.* **71**, 4640–4652 (2011).

48. V.-M. Leppänen, P. Saharinen, K. Alitalo, Structural basis of Tie2 activation and Tie2/Tie1 heterodimerization. *Proc. Natl. Acad. Sci. U. S. A.* **114**, 4376–4381 (2017).

49. K. L. DeCicco-Skinner, G. H. Henry, C. Cataisson, T. Tabib, J. C. Gwilliam, N. J. Watson, E. M. Bullwinkle, L. Falkenburg, R. C. O'Neill, A. Morin, J. S. Wiest, Endothelial cell tube formation assay for the in vitro study of angiogenesis. *J. Vis. Exp.*, e51312 (2014).

50. R. S. Kornbluth, M. Stempniak, G. W. Stone, Design of CD40 agonists and their use in growing B cells for cancer immunotherapy. *Int. Rev. Immunol.* **31**, 279–288 (2012).

51. R. H. Vonderheide, M. J. Glennie, Agonistic CD40 Antibodies and Cancer Therapy. *Clinical Cancer Research*. **19** (2013), pp. 1035–1043.

52. E. R. Steenblock, S. H. Wrzesinski, R. A. Flavell, T. M. Fahmy, Antigen presentation on artificial acellular substrates: modular systems for flexible, adaptable immunotherapy. *Expert Opin. Biol. Ther.* **9**, 451–464 (2009).

53. J. V. Kim, J.-B. Latouche, I. Rivière, M. Sadelain, The ABCs of artificial antigen presentation. *Nat. Biotechnol.* **22**, 403–410 (2004).

54. E. Seydoux, L. J. Homad, A. J. MacCamy, K. R. Parks, N. K. Hurlburt, M. F. Jennewein, N. R. Akins, A. B. Stuart, Y.-H. Wan, J. Feng, R. E. Whaley, S. Singh, M. Boeckh, K. W. Cohen, M. J. McElrath, J. A. Englund, H. Y. Chu, M. Pancera, A. T. McGuire, L. Stamatatos, Analysis of a SARS-CoV-2-Infected Individual Reveals Development of Potent Neutralizing Antibodies with Limited Somatic Mutation. *Immunity*. **53**, 98–105.e5 (2020).

55. C. Wang, W. Li, D. Drabek, N. M. A. Okba, R. van Haperen, A. D. M. E. Osterhaus, F. J. M. van Kuppeveld, B. L. Haagmans, F. Grosveld, B.-J. Bosch, A human monoclonal antibody blocking SARS-CoV-2 infection. *Nat. Commun.* **11**, 2251 (2020).

56. E. Rujas, I. Kucharska, Y. Z. Tan, S. Benlekbir, H. Cui, T. Zhao, G. A. Wasney, P.

Budylowski, F. Guvenc, J. C. Newton, T. Sicard, A. Semesi, K. Muthuraman, A. Nouanesengsy, K. Prieto, S. A. Bueler, S. Youssef, S. Liao-Chan, J. Glanville, N. Christie-Holmes, S. Mubareka, S. D. Gray-Owen, J. L. Rubinstein, B. Treanor, J.-P. Julien, Multivalency transforms SARS-CoV-2 antibodies into broad and ultrapotent neutralizers, , doi:10.1101/2020.10.15.341636.

57. M. A. Tortorici, M. Beltramello, F. A. Lempp, D. Pinto, H. V. Dang, L. E. Rosen, M. McCallum, J. Bowen, A. Minola, S. Jaconi, F. Zatta, A. De Marco, B. Guarino, S. Bianchi, E. J. Lauron, H. Tucker, J. Zhou, A. Peter, C. Havenar-Daughton, J. A. Wojcechowskyj, J. B. Case, R. E. Chen, H. Kaiser, M. Montiel-Ruiz, M. Meury, N. Czudnochowski, R. Spreafico, J. Dillen, C. Ng, N. Sprugasci, K. Culap, F. Benigni, R. Abdelnabi, S.-Y. C. Foo, M. A. Schmid, E. Cameroni, A. Riva, A. Gabrieli, M. Galli, M. S. Pizzuto, J. Neyts, M. S. Diamond, H. W. Virgin, G. Snell, D. Corti, K. Fink, D. Veesler, Ultrapotent human antibodies protect against SARS-CoV-2 challenge via multiple mechanisms. *Science* (2020), doi:10.1126/science.abe3354.

58. L. Piccoli, Y.-J. Park, M. A. Tortorici, N. Czudnochowski, A. C. Walls, M. Beltramello, C. Silacci-Fregni, D. Pinto, L. E. Rosen, J. E. Bowen, O. J. Acton, S. Jaconi, B. Guarino, A. Minola, F. Zatta, N. Sprugasci, J. Bassi, A. Peter, A. De Marco, J. C. Nix, F. Mele, S. Jovic, B. F. Rodriguez, S. V. Gupta, F. Jin, G. Piumatti, G. Lo Presti, A. F. Pellanda, M. Biggiogero, M. Tarkowski, M. S. Pizzuto, E. Cameroni, C. Havenar-Daughton, M. Smithey, D. Hong, V. Lepori, E. Albanese, A. Ceschi, E. Bernasconi, L. Elzi, P. Ferrari, C. Garzoni, A. Riva, G. Snell, F. Sallusto, K. Fink, H. W. Virgin, A. Lanzavecchia, D. Corti, D. Veesler, Mapping Neutralizing and Immunodominant Sites on the SARS-CoV-2 Spike Receptor-Binding Domain by Structure-Guided High-Resolution Serology. *Cell*. **183**, 1024–1042.e21 (2020).

59. D. Pinto, Y.-J. Park, M. Beltramello, A. C. Walls, M. A. Tortorici, S. Bianchi, S. Jaconi, K. Culap, F. Zatta, A. De Marco, A. Peter, B. Guarino, R. Spreafico, E. Cameroni, J. B. Case, R. E. Chen, C. Havenar-Daughton, G. Snell, A. Telenti, H. W. Virgin, A. Lanzavecchia, M. S. Diamond, K. Fink, D. Veesler, D. Corti, Cross-neutralization of SARS-CoV-2 by a human monoclonal SARS-CoV antibody. *Nature*. **583**, 290–295 (2020).

60. A. C. Walls, Y.-J. Park, M. A. Tortorici, A. Wall, A. T. McGuire, D. Veesler, Structure, Function, and Antigenicity of the SARS-CoV-2 Spike Glycoprotein. *Cell*. **181**, 281–292.e6 (2020).

61. K. H. D. Crawford, R. Eguia, A. S. Dingens, A. N. Loes, K. D. Malone, C. R. Wolf, H. Y. Chu, M. A. Tortorici, D. Veesler, M. Murphy, D. Pettie, N. P. King, A. B. Balazs, J. D. Bloom, Protocol and Reagents for Pseudotyping Lentiviral Particles with SARS-CoV-2 Spike Protein for Neutralization Assays. *Viruses*. **12** (2020), doi:10.3390/v12050513.

62. E. Hiramoto, A. Tsutsumi, R. Suzuki, S. Matsuoka, S. Arai, M. Kikkawa, T. Miyazaki, The IgM pentamer is an asymmetric pentagon with an open groove that binds the AIM protein. *Sci Adv*. **4**, eaau1199 (2018).

63. D. Ugurlar, S. C. Howes, B.-J. de Kreuk, R. I. Koning, R. N. de Jong, F. J. Beurskens, J. Schuurman, A. J. Koster, T. H. Sharp, P. W. H. I. Parren, P. Gros, Structures of C1-IgG1 provide insights into how danger pattern recognition activates complement. *Science*. **359**,

794–797 (2018).

Appendix

Amino acid sequences of all successful AbC-forming designs.

Name	Sequence
d2.3	MSDEEERNELIKRIREAAQRAREAAERTGDPRVRELARELARIAQIAFYLVLHDPSSSEVNEALKAVVKAIELAVRALEEAEK TGDPEVRELAREVVRLAVEVATATAAGENDTLRKVAERALRLAKEAAKRGDAKAAKQAAKIAKLAAANAGDEDVLKKVELVR LAIELVEIVVENAKRKGDDDKEAAEAALAAFRIVLAAAQLAGIASLEVLELALRLIKEVVENAQREGYDIAVAAIAAAVAFAVVAV AAAAADITSSEVLELAIRLIKEVVENAQREGYVILLAALAAAAAFVVVAAAAKRAGITSSETLKRAIEEIRKRVEEAQREGNDIS EAARQAAEEFRKKAEELKGSLEHHHHHH
d2.4	MSDEEERNELIKRIREAAQRAREAAERTGDPRVRELARELARIAQIAFYLVLHDPSSSEVNEALKAVVKAIELAVRALEAAEK TGDPRVRELAREVVKAAVDVAEAAQAGLNDKLREVAEKALRLAKEALKEGDSTAAELAAEIARLAAKLAGDEDVLKKVKLVL EAIKLVKIVVENAKRKGDDSKEAAEAAVAAFLIVLAAAKLAGIASEEVLELAARLIKEVVENAQREGYDIAVAAIAAAVAFAVVAV AAAAADITSSEVLELAIRLIKEVVENAQREGYVILLAALAAAAAFVVVAAAAKRAGITSSETLKRAIEEIRKRVEEAQREGNDIS EAARQAAEEFRKKAEELKGSLEHHHHHH
d2.7	MSDEEERNELIKRIREAAQRAREAAERTGDPRVRELARELAKLAQIAFYLVLHDPSAKEVNLALELIVKAIELAVRALEEAEKT GDPHARELAREIVRLAVELARAVAEAAEEAKKQGNSELAEQVARAAQVALEVIKAAITAAKQGDRKAFRAALELVLEVIKAIEE AVKQGNPKKVAEVALKAELIRIVVQNAANKGDDADEAVEAARAAFEIVLAAAQLAGIDSEEVLELAARLIKEVVENAQREGYD IAVAAIAAAVAFAVVAVAAAAADITSSEVLELAIRLIKEVVENAVREGYVILLAALAAAAAFVVVAAAAKRAGITSSETLKRAIEEIR KRVEEAQREGNDISEAARQAAEEFRKKAEELKGSLEHHHHHH
t32.4	MFNKSQQSAFYLILNMPNLNEAQRNGFIQSLKDDPSKSEVVAGEAAIEAARNALKKGSPETAREAVRLALELVQEAERQAR KTGSTERLIAAAKLAIEVARVALKVGSPETAREAVRTALELVQELIRQARKTGSKEVLEEAAKLALEVAKVAAEVGSPETAARA VATAVEALKEAGASEDEIAEIVARVISEVIRILKESGSEYKVICRAVARIVAEIVEALKRSGTSEDEIAEIVARVISEVIRTLKESGS DYLIICVCVAIIVAEIVEALKRSGTSEDEIAEIVARVISEVIRTLKESGSSYEVIKECVQIIVLAIILALMKSGTEVEEILLILLRVKTEV RRTLKESGSLEHHHHHH
t32.8	MFNKDQQSAFYEVLNMPNLNEAQRNGFIQSLKDDPSQSLKILIKAAAGGDSELEEVAKRIVKELAEQGRSEKEAAKEAAELI ERITRAAGGNSDLIELAVRIVKILEEQGRSPSEAAKEAVEAIEAIVRAAGGDSEAIKVAAEIAKTIITQKESGSEYKEICRTVARIV AEIVEKLKRNGASEDEIAEIVAAIIAAVILTLKLSGSDYLIICVCVAIIVAEIVEALKRSGTSEDEIAEIVARVISAVIRVLKESGSSYE VIKECVQIIVLAIILALMKSGTEVEEILLILLRVKTEVRRTLKESGSLEHHHHHH
o42.1	MFNKDQQSAFYEILNMPNLNEALRNGFIQLLKDDPSKSTVILTAAKVAAELSEKIRTLKESGSSYEQIAETVAKAVAKLVEKLK RNGVSEDEIALAVALIISAVIQTLKESGSSYEVIAEIVARIVAEIVEALKRSGTSEDEIAEIVARVISEVIRTLKESGSSYEVIAEIVA RIVAEIVEALKRSGTSEDEIAKIVARVIAEVLRTLKESGSSEEVIKEIVARIITEIKEALKRSGTSEDEIELITLMIEAALEIAKLKSS GSEYEEICEDVARRIAELVEKLKRDGTSAVEIAKIVAAIISAVIAMLKASGSSYEVICECVARIVAEIVEALKRSGTSAAIIALIVALV ISEVIRTLKESGSSFEVILECVIRIVLEIIEALKRSGTSEQDVMLIVMAVLLVVLATLQLSGSLEHHHHHH
i52.3	MSDEEERNELIKRIREAAQRAREAAERTGDPRVRELARELARLAQRAFYLVLHDPSSSDVNEALKLIVEAIEAAVRALEAAER AGDPELREDAREAVRLAVEAAEEVQRNPSSSTANLLLKAIVALAEALAAAANGDKEKFKKAAESALEIAKRVVEVASKEGDP EAVLEAAKVALRVAELAAKNGDKEVFKKAAESALEVAKRLVEVASKEGDPELVLEAAKVALRVAELAAKNGDKEVFQKAAAS AVEVALRLTEVASKEGDSELETEAAKVITRVRELASKQGDAAVAILAETAEVKLEIEESKKRPQSESAKNLILIMQLLINQIRLLV LQIRMLDEQRQEGSLEHHHHHH
i52.6	MSDEEERNELIKRIREAAQRAREAAERTGDPRVRELARELARLAQRAFYLVLHDPSSSDVNEALKLIVEAIEAAVRALEAAER TGDPKVREEARELVRRAVEAAEEVQRNPSSSEVNEKLKAIVVEIEVKVASLEAKEVTDPDKALKIAKKVIELALEAVKENPST EALRAVLEAVRLASEVAKRVTDPDKALKIAKLVIELALEAVKEDPSTDALRAVLEAVRLASEVAKRVTDPDKALKIAKLVLELAA EAVKEDPSTDALRAAKEAERLATEVAKRVTDPKKAREIEMLVLKLQMEAILAETEEVKKEIEESKKRPQSESAKNLILIMQLLIN QIRLLALQIRMLALQLQEGSLEHHHHHH

Amino acid sequences of Fc and Fc-fusions.

Name	Sequence
Fc	METDTLLLWVLLLWVPGSTGHHHHHHGGSENLYFQGGSEPKSSDKTHTCPPCPAPELLGGPSVFLFPPKPKDTLMISRTPEVTCVVVDVSHEDPEVKFNWYVDGVEVHNAKTKPREEQYNSTYRVVSVLTVLHQDWLNGKEYKCKVSNKALPAPIEKTISKAKGQPREPQVYTLPPSRDELTKNQVSLTCLVKGFYPSDIAVEWESNGQPENNYKTTPPVLDSDGSFFLYSKLTVDKSRWQQGNVFSCSVMHEALHNHYTQKSLSLSPGK
GFP-Fc (sfGFP)	SRATMETDTLLLWVLLLWVPGSTGHHHHHHGGSENLYFQGGSSKGEELFTGVVPILVELDGDVNGHKFSVRGEGEGDATNGKLTLKFICTTGKLPVPWPTLVTTLTYGVQCFSRYPDHMKRHDFFKSAMPEGYVQERTISFKDDGTYKTRAEVKFEGDTLVNRIELKGIDFKEDGNILGHKLEYNFNSHNVYITADKQKNGIKANFKIRHNVEDGSVQLADHYQQNTPIGDGPVLLPDNHYLSTQSVLSKDPNEKRDHMVLLEFVTAAGITHGMDELYKGGSGSEPKSSDKTHTCPPCPAPELLGGPSVFLFPPKPKDTLMISRTPEVTCVVVDVSHEDPEVKFNWYVDGVEVHNAKTKPREEQYNSTYRVVSVLTVLHQDWLNGKEYKCKVSNKALPAPIEKTISKAKGQPREPQVYTLPPSRDELTKNQVSLTCLVKGFYPSDIAVEWESNGQPENNYKTTPPVLDSDGSFFLYSKLTVDKSRWQQGNVFSCSVMHEALHNHYTQKSLSLSPGK
RFP-Fc (mRuby2)	SRATMETDTLLLWVLLLWVPGSTGHHHHHHGGSENLYFQGGSVSKGEELIKENMRMKVVMEGSVNGHQFKCTGEGEGNPYMGTQTMRIKVIEGGPLPFAFDILATSFMYGSRTFIKYPKGIPDFFKQSFPEGFTWERVTRYEDGGVVTVMQDTSLEDGCLVYHVQVRGVNFPSNGPVMQKKTKGWEPNTEMMYPADGGLRGYTHMALKVDGGGHLSCSFVTTYRSKKTVGNIKMPGIHAVDHRLERLEESDNEMFVVQREHAVAKFAGLGGGMDELYKGGSGSEPKSSDKTHTCPPCPAPELLGGPSVFLFPPKPKDTLMISRTPEVTCVVVDVSHEDPEVKFNWYVDGVEVHNAKTKPREEQYNSTYRVVSVLTVLHQDWLNGKEYKCKVSNKALPAPIEKTISKAKGQPREPQVYTLPPSRDELTKNQVSLTCLVKGFYPSDIAVEWESNGQPENNYKTTPPVLDSDGSFFLYSKLTVDKSRWQQGNVFSCSVMHEALHNHYTQKSLSLSPGK
A1F-Fc	METDTLLLWVLLLWVPGSTGKAELASEKPFRDCADVYQAGFNKSGIYTIYINNMPEPKKVFCNMDVNGGGWTVIQHREDGSLDFQRGWKEYKMGFGNPSGEYWLGNEFIFAITSQRQYMLRIELMDWEGNRAYSQYDRFHIGNEKQNYRLYLKGHTGTAGKQSSLILHGADFSTKDADNDNCMCKCALMLTGGWWFDACGPSNLNGMFYTAGQNHGKLNGIKWHYFKGPSYSLRSTTMMIRPLDFGGSGGSEPKSSDKTHTCPPCPAPELLGGPSVFLFPPKPKDTLMISRTPEVTCVVVDVSHEDPEVKFNWYVDGVEVHNAKTKPREEQYNSTYRVVSVLTVLHQDWLNGKEYKCKVSNKALPAPIEKTISKAKGQPREPQVYTLPPSRDELTKNQVSLTCLVKGFYPSDIAVEWESNGQPENNYKTTPPVLDSDGSFFLYSKLTVDKSRWQQGNVFSCSVMHEALHNHYTQKSLSLSPGKGGSHHHHHH

Data availability statement. 3D maps from EM have been uploaded to the Electron Microscopy Data Bank (EMDB) with accession numbers EMD-23266 (o42.1 Fc) and EMD-23265 (i52.3 Fc). WORMS code is available in Zenodo at https://zenodo.org/record/4441201. Design models, building blocks, symmetry definition files, and example scripts for making fusions and designing fusion outputs can also be found in Zenodo https://zenodo.org/record/4599680. Statistical information can be found at https://zenodo.org/record/4670723. All other data are available in the corresponding manuscript (*1*).